Revisiting the linear instabilities of plane channel flow between compliant walls

Smail Lebbal, Frédéric Alizard, Benoît Pier

Revisiting the linear instabilities of plane channel flow between compliant walls

Smail LEBBAL, Frédéric ALIZARD, and Benoît PIER

Laboratoire de mécanique des fluides et d'acoustique,

CNRS — École centrale de Lyon — Université de Lyon 1 — INSA Lyon,

36 avenue Guy-de-Collongue, 69134 Écully, France.

(Dated: September 3, 2021)

The present investigation revisits the linear stability of Poiseuille channel flow interacting with compliant walls. The results obtained include the dynamics of Tollmien–Schlichting (TS) modes as well as flow-induced surface-instability (FSI) modes, in the form of both traveling-wave flutter (TWF) and divergence (DIV) modes. The compliant wall model consists of a spring-backed plate with a viscous substrate deformable in the vertical direction (Davies & Carpenter, *J. Fluid Mech.* **352**, 205–243, 1997). At the interface between the fluid and the walls, the continuity of velocities and stresses, including both viscous and pressure contributions, are taken into account. The FSI modes (both varicose and sinuous) and TS modes are then reinterpreted in the light of the two principal nondimensional control parameters: the Reynolds number (Re), which characterizes the base flow, and the reduced velocity (V_R), which measures the response of the flexible wall to hydrodynamic loading (De Langre, *La Houille Blanche*, **3/4**, 14–18, 2000). The characteristics of TS and FSI modes are systematically investigated over a large control-parameter space, including wall dissipation, spring stiffness and flexural rigidity. We observe that TWF modes are primarily governed by V_R and largely independent of the Reynolds number. It is found that the instability is generally dominated by the TWF mode of varicose symmetry. DIV and TS modes are both affected by V_R and Re, confirming that these modes belong to a different class. The onset of the DIV mode is mainly observed for the sinuous motion, when increasing the dissipation. To provide physical insight into the mechanisms driving these instabilities, the perturbative energy equations for both FSI and TS modes are analyzed for a wide range of wall parameters and wavenumbers.

1. INTRODUCTION

The constant scientific interest to extend the laminar regime for industrial applications has led to the development of compliant walls since the beginning of the 20th century. In particular, researchers focused on finding optimum wall properties aiming to delay the laminar–turbulent transition.

In the biological context, interactions between fluid and elastic forces associated with a deformable channel or tube lead to a variety of physiologically significant phenomena. Especially, deformability plays a prominent role in blood flow as well as peristaltic transport, for example through the intestines and the urogenital tract (see[1,2] for a review).

Such interest arose from the so-called Gray's paradox[3]. Indeed, Gray showed that to overcome the friction drag of a swimming dolphin subjected to a turbulent flow around its body, the muscles have to be capable of generating a power at least seven times greater than that of other kinds of mammalian muscle. Hence, Gray has suggested that the dolphin skin is able to delay the laminar–turbulent transition. In the laminar regime, indeed, the power developed by muscles would still conform to that of other types of mammalian muscle.

Kramer[4] in the 50's developed a compliant coating trying to mimic the dolphin's skin. The author claimed that he was able to reduce the drag of a torpedo-like model by as much as 60%. Later, the conclusions of both Gray's hypotheses and Kramer's experiments were in part questioned. Russian and American experiments since the 80's failed to reproduce results provided by Kramer. In addition, scientists observed that the lower turbulence level around the dolphin swimming body could also be attributed to local pressure gradients. It was also suggested that a reduction in the friction drag may result from the fact that the dolphin leaps out of the water for breathing (see[5],[6] and[7] for reviews).

However, Gaster's experiments in 1988[8] gave new hope in using compliant walls to delay laminar–turbulent transition. He showed that the growth rates of artificially generated Tollmien–Schlichting waves are inhibited when using appropriate coatings. These experiments have given a strong impulse to theoretical developments based on linear stability analyses aiming to tackle the fluid–structure interaction problem.

A major difficulty arises from the design of compliant wall models that are able to couple fluid and solid dynamics. These models may be separated into two categories: surface-based or volume-based (see[7,9] for a review). The first class of models is less computationally demanding and considers an infinitely thin wall interacting with the fluid through an interface condition. In this

case, the wall is defined as a thin plate mounted on springs and dampers. The wall parameters are classically the spring stiffness, the tension, the bending stiffness, its mass and damping coefficient.

For the second family of models (*i.e.* volume-based), the wall material is fully described to include single- or multi-layer coatings as well as isotropic or anisotropic behaviours (see the analyses carried out by Patne & Shankar[10] and Kumaran[9] for recent reviews). Duncan[11] has also shown that a one-dimensional model can be used to quantitatively describe many aspects of instabilities and wave propagation on the surface of an elastic and incompressible coating.

In the present investigation we adopt the surface-based approach. Following the lead of Benjamin[12–14] which relies on the theory developed by Miles for water waves[15], Carpenter & Garrad[16,17] focused on the stability of boundary-layer flows over Kramer-type compliant walls. They provided some confirmation of the transition-delaying potential of compliant coatings. According to Carpenter & Garrad[16,17], instability modes can be classified into two categories: fluid-based (Tollmien–Schlichting mode) and solid-based (flow-induced surface instabilities, or fluid–structure instabilities, referenced as FSI hereafter). The last category includes both the traveling-wave flutter (TWF) modes and the (almost static) divergence (DIV) modes. For the divergence mode, scientists are still arguing about its precise nature. It is either interpreted as an absolute instability[18] or it may also result from a modal instability with a nearly vanishing phase velocity when increasing the wall dissipation[19].

In the same fashion, Davies & Carpenter[20] investigated linear instability waves that emerge from the interaction between a compliant channel with a viscous incompressible flow. Considering perturbations of sinuous symmetry, these authors derived a theory for the motion of the walls and obtained neutral stability curves, using wall parameters made dimensionless by quantities associated with the fluid. While such an approach allows to use the Reynolds number as a control parameter for both FSI and TS modes, it is not entirely satisfactory because a change in the Reynolds number also leads to a change in the compliant wall characteristics. A similar study has been recently attempted to address pulsatile Poiseuille flow[21] for modal and nonmodal instabilities.

The purpose of the present paper is to revisit this configuration. Therefore, we reconsider this problem by introducing the so-called reduced velocity to describe FSI modes. A general formulation suitable for both sinuous and varicose symmetries and free of spurious pressure modes is implemented. A wide range of wall parameters has been explored to highlight their influence onto both FSI and TS modes. Only two-dimensional perturbations are considered since the Squire theorem holds for compliant walls[22].

The paper is organized as follows. Section 2 presents the model and governing equations used

for the fluid–structure interaction problem. Especially, the dimensionless parameters and linearized equations will be introduced. Then, section 3 provides some physical insight into the influence of wall parameters onto FSI and TS modes for both the sinuous and varicose symmetries. For that purpose, kinetic energy budgets are computed. Conclusions and prospects are given in the last section.

2. PROBLEM FORMULATION

2.1. Fluid–structure interaction model and interface conditions

In the entire paper, we restrict our analysis to the two-dimensional problem. Using a Cartesian coordinate system (x, y) with unit vectors $(\mathbf{e_x}, \mathbf{e_y})$, we consider an incompressible, Newtonian fluid with dynamic viscosity μ and density ρ between two spring-backed deformable plates located at $y = \zeta^{\pm}(x,t)$, which are allowed to move only in the y-direction. A schematic diagram of the configuration is shown in figure 1.

The flow between the walls is governed by the Navier–Stokes equations:

$$\begin{aligned} &\frac{\partial \mathbf{u}}{\partial t} + (\mathbf{u}\cdot\nabla)\mathbf{u} = -\frac{1}{\rho}\nabla p + \nu\Delta\mathbf{u}, \\ &\nabla\cdot\mathbf{u} = 0, \end{aligned} \tag{1}$$

where $\mathbf{u} = (u, v)$ and p represent the velocity and pressure fields, and u (resp. v) denotes the streamwise (resp. wall-normal) velocity component, and $\nu \equiv \mu/\rho$ is the kinematic viscosity of the fluid.

The movement of the flexible plates obeys the following equations, derived through Newton's second law:

$$m\frac{\partial^2\zeta^{\pm}}{\partial t^2} + d\frac{\partial\zeta^{\pm}}{\partial t} + \left(B\frac{\partial^4}{\partial x^4} - T\frac{\partial^2}{\partial x^2} + K\right)\zeta^{\pm} = f^{\pm}. \tag{2}$$

Here, m denotes the mass per unit area of the plates, d their damping coefficient, B the flexural rigidity, T the wall tension, K the spring stiffness and $f^{\pm}$ represents the y-component of the hydrodynamic forces acting on the plates. These forces are obtained as

$$f^{\pm} = \mathbf{e_y}\cdot\mathbf{f}^{\pm} \quad \text{with} \quad \mathbf{f}^{\pm} = \left(\overline{\overline{\tau}}^{\pm} - \delta p^{\pm}\mathbf{I}\right)\cdot\mathbf{n}^{\pm}. \tag{3}$$

Here $\overline{\overline{\tau}}^{\pm}$ denotes the viscous stress tensor at the walls and $\delta p^{\pm}$ the transmural surface pressure, *i.e.*, the difference between the surface pressure inside and outside of the channel, and $\mathbf{n}^{\pm}$ is the unit vector normal to the walls pointing towards the fluid.

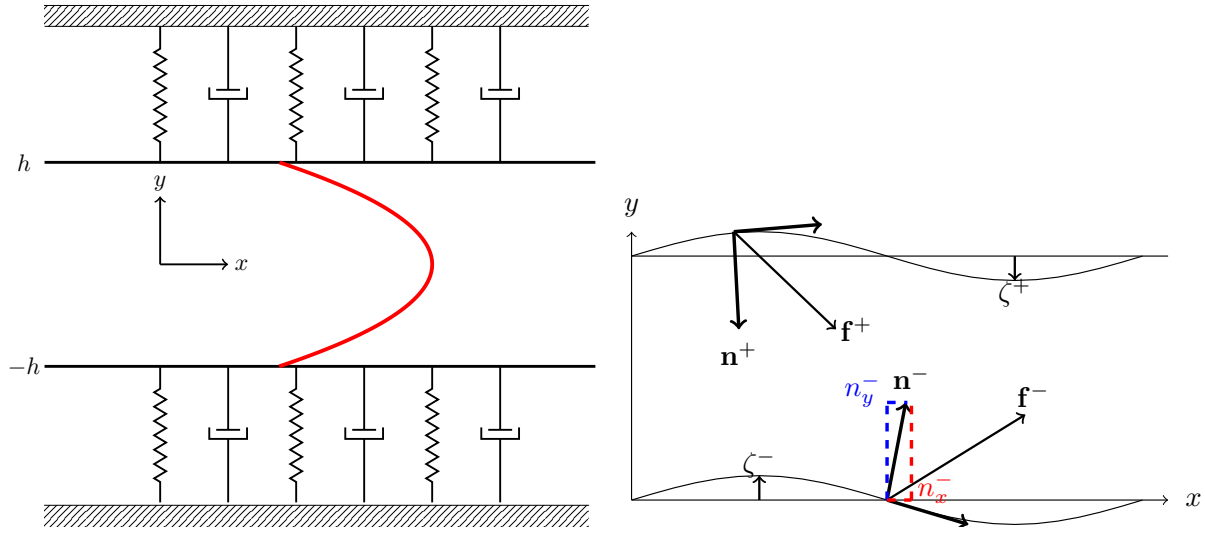

(a) Schematic diagram showing the equilibrium state configuration.

(b) Wall deformation and coordinate systems.

FIG. 1: Channel flow with infinite spring-backed flexible walls.

The viscous stress tensor at the walls has the following expression:

$$\overline{\overline{\tau}}^{\pm} = \left(\begin{array}{cc} 2\mu\dfrac{\partial u}{\partial x} & \mu\left(\dfrac{\partial u}{\partial y}+\dfrac{\partial v}{\partial x}\right) \\ \mu\left(\dfrac{\partial u}{\partial y}+\dfrac{\partial v}{\partial x}\right) & 2\mu\dfrac{\partial v}{\partial y} \end{array} \right)\Bigg|_{y=\zeta^{\pm}}, \tag{4}$$

and the normal vectors to the interface $\mathbf{n}^{\pm} = \left(n_x^{\pm}, n_y^{\pm}\right)$ are obtained as

$$n_x^{\pm} = \pm\frac{\partial \zeta^{\pm}}{\partial x}\frac{1}{\sqrt{1+\left(\frac{\partial \zeta^{\pm}}{\partial x}\right)^2}} \quad \text{and} \quad n_y^{\pm} = \mp\frac{1}{\sqrt{1+\left(\frac{\partial \zeta^{\pm}}{\partial x}\right)^2}}. \tag{5}$$

Combining (3,4,5) yields the y-component of the hydrodynamic forces acting on the compliant walls

$$f^{\pm} = \left[\pm\mu\left(\left.\frac{\partial u}{\partial y}\right|_{y=\zeta^{\pm}} + \left.\frac{\partial v}{\partial x}\right|_{y=\zeta^{\pm}}\right)\zeta_x^{\pm} \mp 2\mu\left.\frac{\partial v}{\partial y}\right|_{y=\zeta^{\pm}} \pm \delta p^{\pm}\right] \Bigg/ \sqrt{1+\left(\frac{\partial \zeta^{\pm}}{\partial x}\right)^2}, \tag{6}$$

which governs the wall dynamics (2) since the wall-movement is constrained to occur only in the y-direction. Note that in this approach there are no hydrodynamic forces acting on the plate from the outside, except a pressure.

Finally, the no-slip conditions on both walls lead to the kinematic conditions prevailing at the moving boundaries:

$$u = 0 \quad \text{and} \quad v = \frac{\partial \zeta^{\pm}}{\partial t} \quad \text{for} \quad y = \zeta^{\pm}. \tag{7}$$

Thus, the fluid–structure interaction problem is completely determined by the coupling of the fluid equations (1), the wall equations (2) and boundary conditions (7).

2.2. Dimensionless control parameters

The present compliant-channel flow configuration is characterized by 9 dimensional parameters: the volumetric flow rate $[Q] = \mathrm{m}^3\mathrm{s}^{-1}$, the half height $[h] = \mathrm{m}$ of the channel, the fluid density $[\rho] = \mathrm{kg\,m}^{-3}$, the kinematic viscosity $[\nu] = \mathrm{m}^2\mathrm{s}^{-1}$, the mass of the plate per unit area $[m] = \mathrm{kg\,m}^{-2}$, the damping coefficient of the wall $[d] = \mathrm{kg\,m}^{-2}\mathrm{s}^{-1}$, the bending stiffness of the plate $[B] = \mathrm{kg\,m}^2\mathrm{s}^{-2}$, the wall tension $[T] = \mathrm{kg\,s}^{-2}$ and the spring stiffness $[K] = \mathrm{kg\,m}^{-2}\mathrm{s}^{-2}$. Hence, this system may be described by 6 dimensionless parameters. A useful parameter to characterize fluid–structure interaction phenomena is the reduced flow velocity V_R, defined[23] as the ratio of a characteristic time of the structure to a characteristic time of the flow. Using time scales based on spring stiffness

$$\tau_K = \sqrt{\frac{m}{K}}$$

and flow advection

$$\tau_Q = \frac{4h^2}{Q},$$

the reduced velocity is obtained as $V_R = \tau_K/\tau_Q$. Other choices based on different characteristic times would be possible. For $V_R \ll 1$, the influence of the wall compliance is negligible, while $V_R \gg 1$ corresponds to very soft walls. Hence, the resulting 6 nondimensional control parameters are

$$\begin{cases} Re = \dfrac{Q}{\nu}, \quad V_R = \dfrac{Q}{4h^2}\sqrt{\dfrac{m}{K}}, \quad \Gamma = \dfrac{m}{\rho h}, \\[2ex] d_* = \dfrac{d}{\sqrt{mK}}, \quad B_* = \dfrac{B}{Kh^4}, \quad T_* = \dfrac{T}{h^2K}. \end{cases} \tag{8}$$

Here Re is the Reynolds number based on channel diameter and average flow velocity, and Γ is the mass ratio between the compliant walls and the fluid. The three nondimensional wall parameters d_*, B_* and T_* are all relative to the spring stiffness K, which serves as reference for the reduced velocity V_R. One may notice that in several previous studies[20,24,25], fluid quantities are used to build nondimensional parameters for the wall. As underlined by Domaradzki & Metcalfe[26], this may correspond to nonphysical situations where at each Reynolds number a different compliant wall and a different fluid are considered. In the present work, the Reynolds number may be

modified using ν and/or Q without changing the wall properties. Hereafter, the mass ratio is kept constant at $\Gamma = 2$ and we only consider walls without tension $T = 0$. We fix the three dimensional parameters at $\rho = 1$, $h = 1$ and $\tau_Q = 1$.

2.3. Formulation of the linearized model

This entire study considers the dynamics of small-amplitude perturbations, obeying the linearized version of the governing equations around a steady base state. The unperturbed base configuration thus consists of a parabolic Poiseuille flow $\mathbf{U}(y) = (U_b(y), 0)$ between parallel walls located at $y = \pm h$ (see figure 1a). This flow is driven by a pressure $P_b(x) = P_0 - Gx$ of constant streamwise gradient, and we assume a pressure outside the channel membranes always equal to $P_b(x)$, so as to equilibrate the forces acting on both sides of the membranes for unperturbed conditions.

The total flow fields are then decomposed as $\mathbf{u}(x, y, t) = \mathbf{U}(y) + \mathbf{u}'(x, y, t)$ and $p\,(x, y, t) = P_b(x) + p'\,(x, y, t)$. The wall displacement is written as $\zeta^{\pm}(x, t) = \pm h + \eta^{\pm}(x, t)$.

Considering that the perturbation components $\mathbf{u}'$, p' and $\eta^{\pm}$ are of small amplitude, the governing equations may be linearized about the base state.

Since the base state is steady and homogenous in the streamwise direction, the perturbation to the velocity fields, pressure fields and normal displacements are expressed in normal-mode form as:

$$\mathbf{u}'\,(x, y, t) = \hat{\mathbf{u}}(y)e^{i(\alpha x - \omega t)}, \quad p'\,(x, y, t) = \hat{p}(y)e^{i(\alpha x - \omega t)} \quad \text{and} \quad \eta^{\pm}\,(x, t) = \hat{\eta}^{\pm}e^{i(\alpha x - \omega t)}, \tag{9}$$

with α the streamwise wavenumber and ω the frequency. Hereafter, we adopt a temporal view point where $\alpha \in \mathbb{R}$ and $\omega = \omega_r + i\omega_i \in \mathbb{C}$, with ω_i the temporal amplification rate of the mode and ω_r its circular frequency. Substitution of this decomposition into the Navier–Stokes equations and linearization about the base flow leads to:

$$\begin{cases} -i\omega\rho\hat{u} + \rho i\alpha\hat{u}U_b + \rho\hat{v}\dfrac{dU_b}{dy} = -i\alpha\hat{p} + \mu\left(\dfrac{d^2}{dy^2} - \alpha^2\right)\hat{u}, \\ \\ -i\omega\rho\hat{v} + \rho i\alpha\hat{v}U_b \qquad\quad = \quad -\dfrac{d\hat{p}}{dy} + \mu\left(\dfrac{d^2}{dy^2} - \alpha^2\right)\hat{v}, \end{cases} \tag{10}$$

together with the divergence-free condition:

$$i\alpha\hat{u} + \frac{d\hat{v}}{dy} = 0. \tag{11}$$

Linearization of the wall equations (2,6) yields

$$\begin{cases} -\omega^2 m\hat{\eta}^+ - i\omega d\hat{\eta}^+ + \left(B\alpha^4 + T\alpha^2 + K\right)\hat{\eta}^+ = +\hat{p}\left(h\right) - \mu\left(i\alpha\dfrac{dU_b}{dy}\bigg|_h \hat{\eta}^+\right) - 2\mu\dfrac{d\hat{v}}{dy}\bigg|_{+h}, \\ \\ -\omega^2 m\hat{\eta}^- - i\omega d\hat{\eta}^- + \left(B\alpha^4 + T\alpha^2 + K\right)\hat{\eta}^- = -\hat{p}\left(-h\right) - \mu\left(i\alpha\dfrac{dU_b}{dy}\bigg|_{-h} \hat{\eta}^-\right) + 2\mu\dfrac{d\hat{v}}{dy}\bigg|_{-h}. \end{cases} \tag{12}$$

Following Shankar & Kumaran[27], the boundary conditions at the perturbed interface are implemented using Taylor series about the base state at $y = \pm h$. At linear order, the flow velocity at the walls reads:

$$\mathbf{u}\left(x, y = \zeta^{\pm}, t\right) = \mathbf{u}'\left(x, y = \pm h, t\right) + \eta^{\pm}\frac{dU_b}{dy}\bigg|_{\pm h}\mathbf{e_x}. \tag{13}$$

Thus, the kinematic boundary conditions (7) become

$$\hat{u}\left(\pm h\right) + \hat{\eta}^{\pm}\frac{dU_b}{dy}\bigg|_{\pm h} = 0 \quad \text{and} \quad \hat{v}\left(\pm h\right) = -i\omega\hat{\eta}^{\pm}. \tag{14}$$

Then, by using (14) and the divergence-free condition, the right-hand-side of (12) can be further simplified, leading to:

$$\begin{cases} -\omega^2 m\hat{\eta}^+ - i\omega d\hat{\eta}^+ + \left(B\alpha^4 + T\alpha^2 + K\right)\hat{\eta}^+ = +\hat{p}\left(h\right) - \mu\dfrac{d\hat{v}}{dy}\bigg|_h, \\ \\ -\omega^2 m\hat{\eta}^- - i\omega d\hat{\eta}^- + \left(B\alpha^4 + T\alpha^2 + K\right)\hat{\eta}^- = -\hat{p}\left(-h\right) + \mu\dfrac{d\hat{v}}{dy}\bigg|_{-h}. \end{cases} \tag{15}$$

Equations (10), (11) and (15) completely govern the dynamics of small-amplitude perturbations and take into account the linearized fluid–structure coupling as derived from the exact hydrodynamic forces.

3. NUMERICAL METHODS

In this work, we follow the general framework described by Manning *et al.* [28] for avoiding spurious eigenvalues. First of all, we rewrite (15) using velocity components at the boundaries. For illustration purposes, only the upper wall is here considered.

Using the condition $-i\omega\hat{\eta}^+ = \hat{v}(h)$, we obtain

$$-i\omega\hat{v}\left(h\right) = W_1\hat{v}\left(h\right) + W_2\hat{u}\left(h\right) + \frac{1}{m}p\left(h\right), \tag{16}$$

with

$$W_1 = -\frac{d}{m} - 2\frac{\mu}{m}\frac{d}{dy} \quad \text{and} \quad W_2 = \frac{\left(B\alpha^4 + T\alpha^2 + K\right)}{m\frac{dU_b}{dy}\Big|_h} + \frac{\mu}{m}i\alpha.$$

The kinematic condition $\hat{u}(h) + \hat{\eta}^{+} \left.\frac{dU_b}{dy}\right|_h = 0$ is recast as

$$-i\omega\hat{u}(h) + \hat{v}(h) \left.\frac{dU_b}{dy}\right|_h = 0. \tag{17}$$

The velocity components and pressure are discretized in the y-direction using a Chebyshev collocation method. To avoid spurious pressure modes, we consider the so-called $\mathbb{P}_N - \mathbb{P}_{N-2}$ approximation in which the pressure is approximated with a polynomial of degree $N-2$ while the velocity is discretized with a polynomial of degree N[29]. From this point, we note the vectors containing the unknowns: $\mathbf{V} = \left(\overbrace{\hat{u}_0, \hat{u}_N, \hat{v}_0, \hat{v}_N}^{\mathbf{V_{BC}}}, \overbrace{\hat{u}_1 \ \ldots \ \hat{u}_{N-1}, \hat{v}_1 \ \ldots \ \hat{v}_{N-1}}^{\mathbf{V_I}} \right)$ and $\mathbf{P_I} = (\hat{p}_1 \ \ldots \ \hat{p}_{N-1})$, where we separate the boundary values ($\mathbf{V_{BC}}$) from the interior points ($\mathbf{V_I}$). Hence, the discretized counterpart of the previous continuous model (10, 15, 14) reads:

$$\overbrace{\phantom{\mathbf{A_1}}}^{4} \ \overbrace{\phantom{\mathbf{A_2}}}^{2(N-2)} \ \overbrace{\phantom{\mathbf{A_3}}}^{N-2}$$

$$\begin{bmatrix} \mathbf{A_1} & \mathbf{A_2} & \mathbf{A_3} \\ \mathbf{B_1} & \mathbf{B_2} & \mathbf{B_3} \\ \mathbf{0} & \mathbf{C_2} & \mathbf{0} \end{bmatrix} \begin{bmatrix} \mathbf{V_{BC}} \\ \mathbf{V_I} \\ \mathbf{P_I} \end{bmatrix} = i\omega \begin{bmatrix} \mathbf{I} & \mathbf{0} & \mathbf{0} \\ \mathbf{0} & \mathbf{I} & \mathbf{0} \\ \mathbf{0} & \mathbf{0} & \mathbf{0} \end{bmatrix} \begin{bmatrix} \mathbf{V_{BC}} \\ \mathbf{V_I} \\ \mathbf{P_I} \end{bmatrix} \begin{matrix} \} 4 \\ \} 2(N-2) \\ \} N-2 \end{matrix}, \tag{18}$$

where the divergence-free condition is imposed on the interior points and $\mathbf{I}$ denotes the identity matrix. The derivative matrices based on Chebyshev polynomials are either expressed on the interior points only (for the pressure) or all the nodes (for the velocity components)[29]. Note that the boundary equations involve the pressure at $y = \pm h$: these values are readily obtained by polynomial interpolation with spectral accuracy, corresponding to matrix $\mathbf{A_3}$.

The discrete counterpart of the divergence-free condition reads $\mathbf{C_2 V_I} = \mathbf{0}$. Hence, from

$$\mathbf{0} = \mathbf{C_2}(i\omega\mathbf{V_I}) = \mathbf{C_2 B_1 V_{BC}} + \mathbf{C_2 B_2 V_I} + \mathbf{C_2 B_3 P_I},$$

the vector $\mathbf{P_I}$ can be expressed as a function of $\mathbf{V_I}$ and $\mathbf{V_{BC}}$:

$$\mathbf{P_I} = \overbrace{-\left(\mathbf{C_2 B_3}\right)^{-1} \mathbf{C_2 B_1}}^{\mathbf{M_{BC}}} \mathbf{V_{BC}} \overbrace{-\left(\mathbf{C_2 B_3}\right)^{-1} \mathbf{C_2 B_2}}^{\mathbf{M_I}} \mathbf{V_I}.$$

Thus eliminating the pressure, the system (18) is recast as

$$\begin{bmatrix} \mathbf{A_1} + \mathbf{A_3 M_{BC}} & \mathbf{A_2} + \mathbf{A_3 M_I} \\ \mathbf{B_1} + \mathbf{B_3 M_{BC}} & \mathbf{B_2} + \mathbf{B_3 M_I} \end{bmatrix} \begin{bmatrix} \mathbf{V_{BC}} \\ \mathbf{V_I} \end{bmatrix} = i\omega \begin{bmatrix} \mathbf{I} & \mathbf{0} \\ \mathbf{0} & \mathbf{I} \end{bmatrix} \begin{bmatrix} \mathbf{V_{BC}} \\ \mathbf{V_I} \end{bmatrix}. \tag{19}$$

The system (19) still contains $N-2$ null eigenvalues due to the divergence-free constraint. We can further reduce (19) by eliminating the streamwise velocity components at the interior points[28]. Indeed, using $\mathbf{V_I} = \left(\overbrace{\hat{u_1}, \quad ... \quad , u_{\hat{N-1}}}^{\mathbf{U}}, \overbrace{\hat{v_1}, \quad ... \quad , v_{\hat{N-1}}}^{\mathbf{V}} \right)$, the divergence-free condition $\mathbf{C_2 V_I} = 0$ becomes $i\alpha \mathbf{U} + \mathbf{C_{2V}} \mathbf{V} = 0$. Thus, for $\alpha \neq 0$, the streamwise velocity $\mathbf{U}$ is obtained as a function of $\mathbf{V}$. This then leads to a discrete version of the Orr–Sommerfeld equation for the fluid–structure interaction problem of the form:

$$\begin{bmatrix} \bullet & \bullet \\ \bullet & \bullet \end{bmatrix} \begin{bmatrix} \mathbf{V_{BC}} \\ \mathbf{V} \end{bmatrix} = i\omega \begin{bmatrix} \mathbf{V_{BC}} \\ \mathbf{V} \end{bmatrix}. \tag{20}$$

This system may be further reduced[30], by considering perturbations of either sinuous or varicose symmetry and using only half of the channel together with derivative operators appropriate for the symmetry of each component of the different flow fields.

Apart from the fact that the above algebraic transformations remove spurious eigenvalues, they also drastically reduce the computational effort. The system is either solved using QZ algorithm from the Lapack library or an Arnoldi technique provided by the Arpack software. The numerical procedure is validated and discussed in Appendix 1. The number of collocation points is varied from 100 to 300 as the Reynolds number is increased.

4. LINEAR STABILITY RESULTS

After the formulation of the linear fluid–structure interaction problem and the presentation of the numerical methods, we are now in a position to analyze its dynamics. The different classes of modes and their dependence on the control parameters are investigated in detail. A specific attention is devoted to provide physical insight through total energy budget analyses.

4.1. Spectra and classes of modes

A typical spectrum is shown in figure 2, corresponding to a base configuration at $Re = 7000$, $V_R = 1$, $B_\star = 4$, $d_\star = 0.2$ and perturbations with wavenumber $\alpha = 0.6$. Since the base state is symmetric in y, the entire spectrum consists of the same number of modes of either varicose (red symbols) or sinuous (blue) symmetry. The Orr–Sommerfeld modes ($\times$ and $+$) are essentially due to the base Poiseuille flow and organized in three branches (classically labelled A, P and S[31]), as

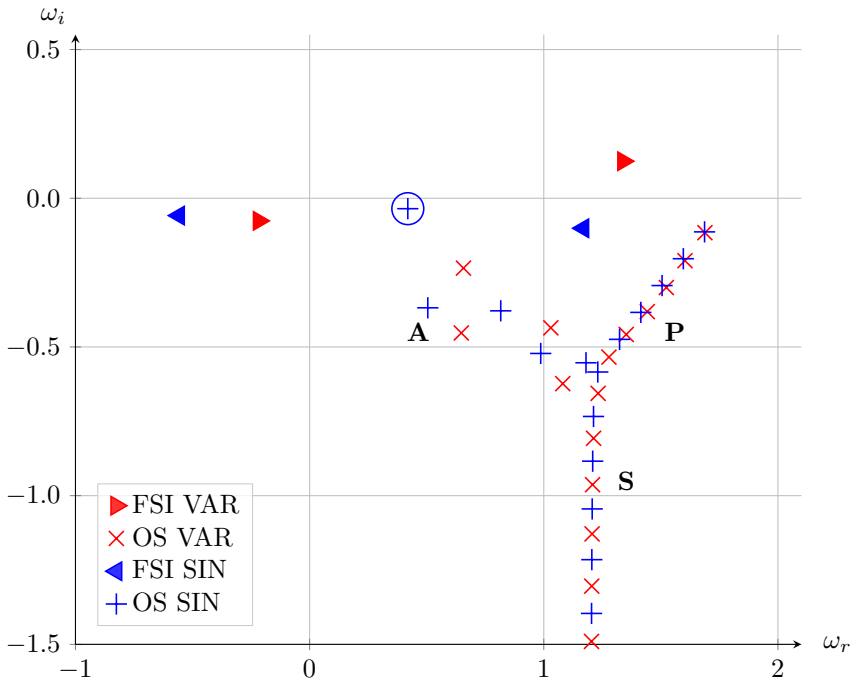

FIG. 2: Eigenvalue spectrum for perturbations with $\alpha = 0.6$ at $Re = 7000$, $V_R = 1$, $B_\star = 4$ and $d_\star = 0.2$. Orr–Sommerfeld modes (+ sinuous and × varicose) are located on three main branches (A, P and S) and dominated by TS mode (circle); four modes ($\triangleleft$ and $\triangleright$) are due to fluid–structure interactions. Modes of varicose and sinuous symmetry are shown in red and blue respectively.

for rigid channels. This part of the spectrum is dominated by the Tollmien–Schlichting mode (TS, indicated by circle in figure 2) of sinuous symmetry. In the present configuration, the coupling between the fluid and wall equations leads to four additional eigenvalues (indicated by $\triangleleft$ and $\triangleright$) and referenced hereafter as fluid–structure interaction (FSI) modes. Two of these FSI modes travel upstream ($\omega_r < 0$), while the other pair of FSI modes propagates along the flow direction ($\omega_r > 0$); each of these pairs consists of a sinuous and a varicose mode.

To gain a better understanding of these eigenmodes, we monitor changes in the spectrum resulting from the variation of some control parameters. A few typical scenarios are shown in figure 3.

FSI modes strongly depend on the reduced velocity V_R, as shown in figure 3(a). When $V_R \to 0$, which corresponds to approaching the rigid-walls case, the growth rates of the FSI modes reach neutrality ($\omega_i \to 0$) while their phase velocities tend to infinity ($\omega_r \to \pm\infty$). For the range of base

state configurations shown here, the upstream propagating FSI modes are always stable, albeit with a weak decay rate, and their (negative) phase velocities reach very small values as V_R is increased: this behaviour is characteristic of divergence (DIV) modes, as observed for boundary-layer flows along highly damped walls[19]. On the other hand, the downstream propagating FSI modes are strongly destabilized as V_R is increased; these modes are identified as traveling-wave flutter (TWF) modes. In contrast with the FSI mode dynamics, the TS mode only weakly depends on V_R since it is mainly driven by the shear flow, see insert in figure 3(a). Consistently with the definition of V_R, the eigenvalue corresponding to the TS mode matches the one found for the rigid case when $V_R \to 0$. The other Orr–Sommerfeld modes on the A-branch also display only a weak dependence on V_R, while those on the P- and S-branches appear to be mostly unaffected.

The influence of the wall-damping parameter $d_\star$ is shown in figure 3(b,c) for $V_R = 1$ (b) and $V_R = 2$ (c). The growth rate ω_i of the downstream propagating TWF modes is seen to significantly decrease with wall dissipation $d_\star$. Thus wall damping has a strongly stabilizing effect on both sinuous and varicose TWF modes. For $V_R = 1$, figure 3(b) shows that wall damping has a similar stabilizing effect on the upstream propagating FSI modes. However, at the larger value $V_R = 2$ of the reduced velocity (figure 3c), these FSI modes are nearly stationary divergence modes. In that regime, an increase in wall damping $d_\star$ results in an increase of their negative growth rate, and the phase velocity is seen to vanish in the limit of large wall damping $d_\star$. Here destabilisation of the DIV modes occurs for large values of $d_\star$. One may recall that while the sinuous TWF and DIV modes were investigated numerically by Davies & Carpenter[20], the varicose TWF and DIV modes have not been explored for the plane channel flow.

Thus, the influence of the various control parameters may be summarized as follows: the TS mode is temporally damped by an increase of V_R, but its temporal amplification rate may be amplified with an increase in wall damping for a certain range of streamwise wave numbers. A different behavior is found when the TWF modes are considered: their growth rate increases with V_R, while it decreases with $d_\star$. This is consistent with the mode classification given by Benjamin[14] (*i.e.* class A for TS modes and class B for TWF modes). Moreover, the DIV modes are seen to be amplified for high values of wall damping parameter. Finally, the effect of the wall compliance is seen to be negligible for both P- and S-branches.

To further identify the different types of modes with respect to Benjamin's classification, the eigenfunctions of a few selected modes are shown in figure 4.

One may recall that the mechanism whereby both TWF modes and TS modes grow involves the action of the streamwise velocity base flow gradient along the wall-normal position working

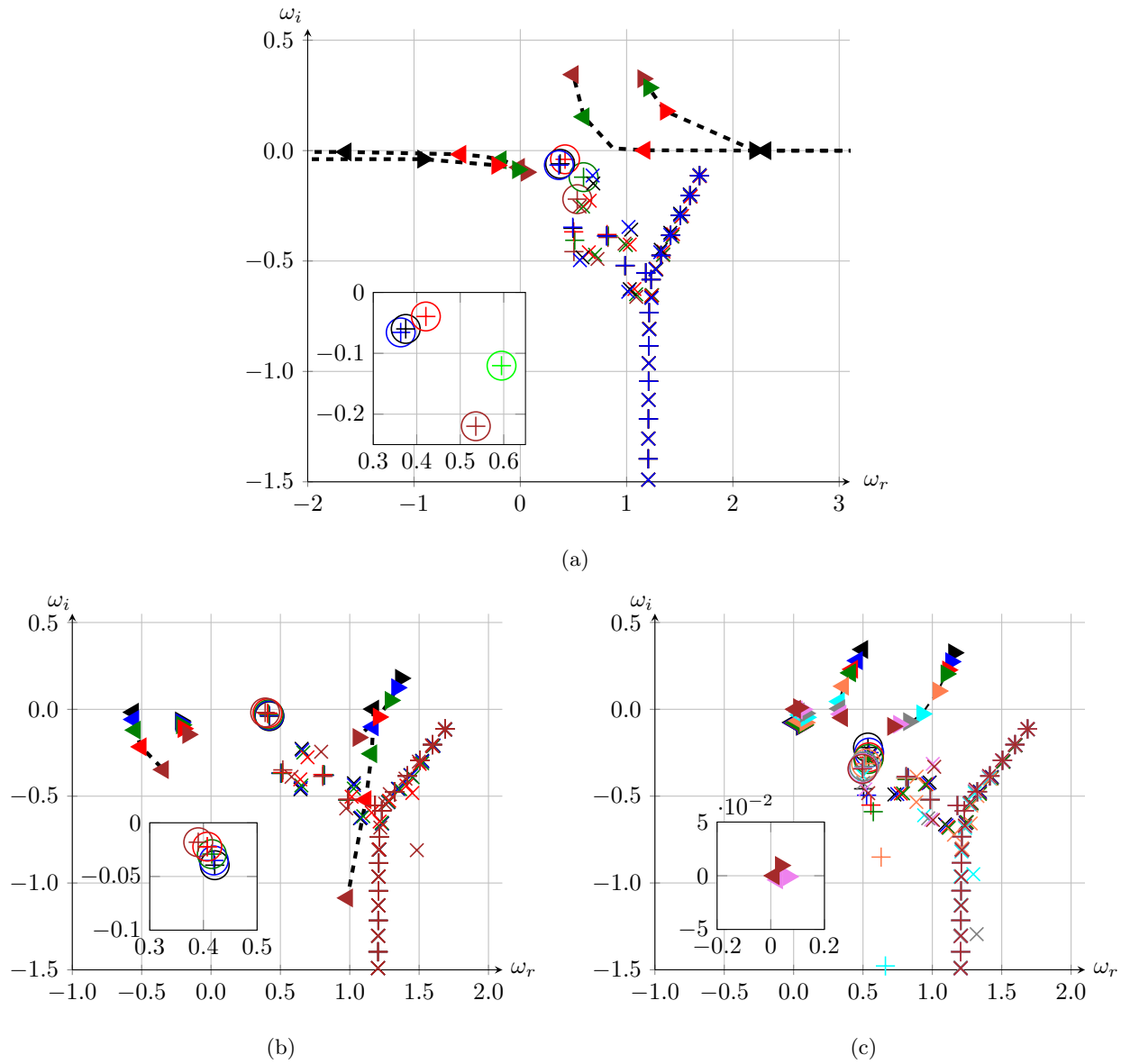

FIG. 3: Influence of reduced velocity V_R and wall damping $d_\star$ on frequency eigenspectra for $\alpha = 0.6$ at $Re = 7000$ and $B_\star = 4$. (a) Evolution with $V_R = 2,\ 1.5,\ 1,\ 0.5,\ 0.01$ (in brown, green, red, black and blue, respectively) at $d_\star = 0$. (b) Evolution with $d_\star$ varying from 0 to 2 for $V_R = 1$ ($d_\star = 0,\ 0.2,\ 0.5\ 1$ and 2 in black, blue, green, red and brown, respectively). (c) Evolution with $d_\star$ varying from 0 to 20 for $V_R = 2$ ($d_\star = 0,\ 0.4,\ 0.8,\ 1, 2,\ 4,\ 6,\ 10$ and 20 in black, blue, red, green, orange, light blue, grey, pink and brown, respectively). Some mode trajectories are represented in dashed lines.

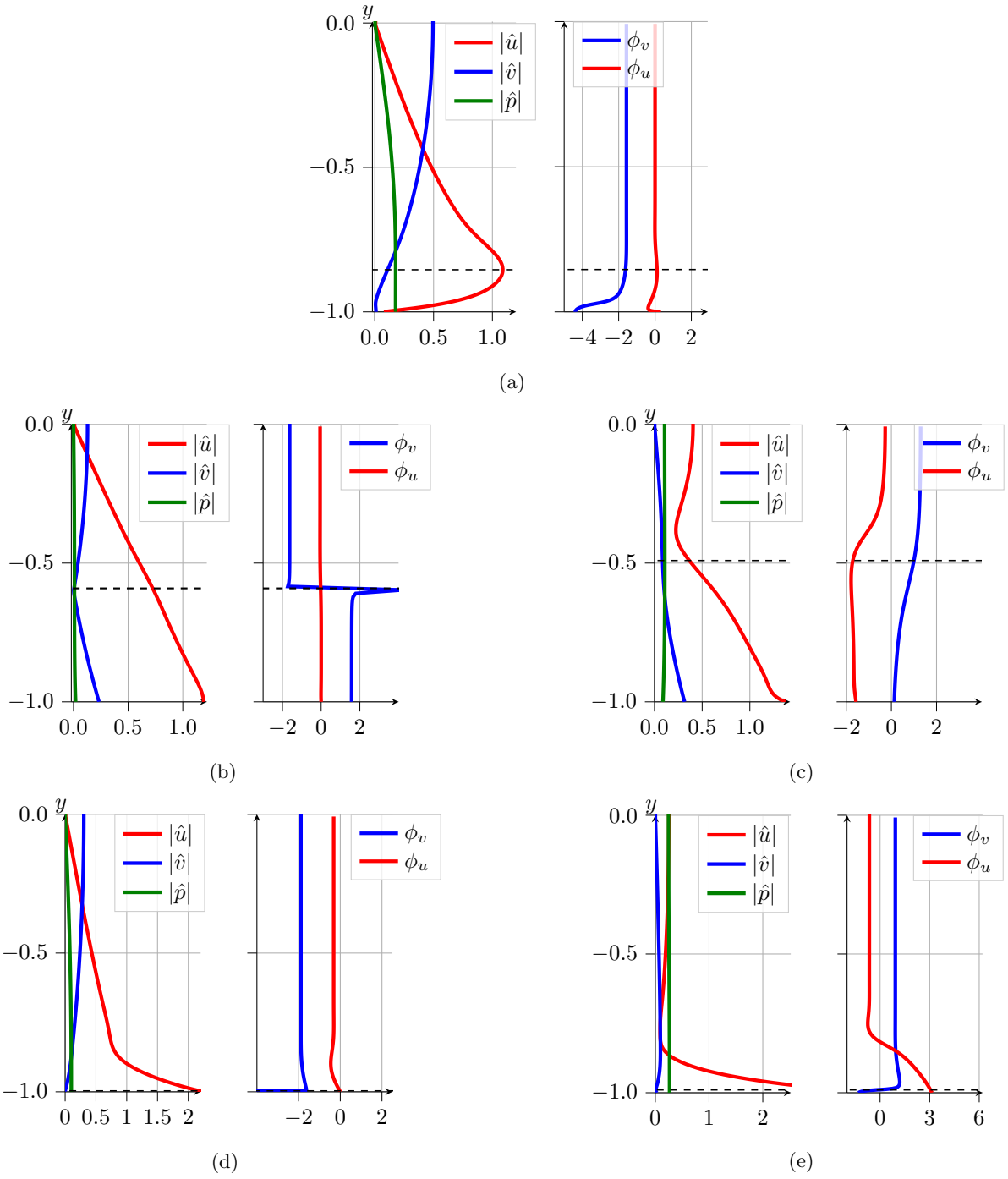

FIG. 4: Eigenfunctions for $Re = 7000$ and $B_\star = 4$. (a) TS (sinuous) mode for $\alpha = 1$, $d_\star = 4$ and $V_R = 0.5$. (b) Sinuous TWF mode for $\alpha = 0.6$, $d_\star = 0$ and $V_R = 1$. (c) Varicose TWF mode for $\alpha = 0.6$, $d_\star = 0$ and $V_R = 1$. (d) Sinuous DIV mode for $\alpha = 0.6$, $d_\star = 20$ and $V_R = 2$. (e) Varicose DIV mode for $\alpha = 0.6$, $d_\star = 20$ and $V_R = 2$. The phase angles of eigenfunctions are denoted as ϕ_u and ϕ_v for u' and v', respectively. The eigenfunctions are normalized to unit kinetic energy norm.

against the Reynolds stresses. In the absence of an inflection point, both modes involve a phase shift of the disturbance velocity at some distance from the wall[32]. However, mechanisms are quite different for each of these modes. Within a large-Reynolds-number asymptotic theory, viscous effects are only present in the vicinity of the viscous wall-layer or the critical layer, located at the wall-normal position y_c where $U_b(y_c) = \omega_r/\alpha$[32]. The inviscid approximation is therefore accurate in the other regions of the flow. For the TWF mode, the instability mechanism is essentially driven by the wall. Indeed, the instability is amplified if the work done by the pressure disturbance on the wall is positive when averaged over one period (Benjamin[12]). As first proven by Miles[15] for water waves, Benjamin[13] shows for the boundary-layer-flow case that it results from a phase shift between disturbance wall pressure and wall displacement. In particular, Benjamin[13] proves that the pressure at the wall is associated with the integrated effect of the velocity perturbations along the wall direction and is a consequence of a phase shift for velocity components near the critical layer. We note hereafter ϕ_u and ϕ_v the phases of the respective velocity components $\hat{u}$ and $\hat{v}$ of the associated eigenfunctions. For TWF modes (see figures 4b,c), the essential phase shift (*i.e.* $\phi_u - \phi_v \neq \pi/2$) occurs near the critical layer in the limit of large Reynolds numbers (class B modes). For the TS mode (figure 4a), the phase shift is rather associated with the viscous wall layer. They belong to class A modes and are stabilized through a transfer of energy to the wall. Hence it is essential, when addressing the different classes of modes, to monitor the phases of the perturbation components. Figure 4(b) shows that the sinuous TWF mode exhibits a clear phase shift near the critical layer in agreement with class B modes. It is consistent with the theoretical investigation of Davies & Carpenter[20] for the same flow case. The linear behaviour along with the wall normal position of $\hat{u}$ is associated with a displacement of the Poiseuille solution when the walls are shifted with η. It is easily verified that the small deviation from the Poiseuille solution due to sinuous motion of the walls is proportional to $-2\hat{\eta}y$ (see also[33]). Interestingly, the varicose case (figure 4c), not studied by Davies & Carpenter[20], also exhibits a phase shift.

Finally, the divergence mode (figure 4d,e) exhibits a phase shift in the viscous wall layer. Nevertheless, due to the low velocity phase, the viscous wall layer and the critical layer are not well separated. As a consequence, the theoretical framework derived by Davies & Carpenter[20] cannot be applied for these modes.

For all FSI modes (both TWF and DIV), velocity and pressure fluctuations are concentrated near the wall. For the TS mode, as for the rigid case, the streamwise velocity component peaks at the critical layer.

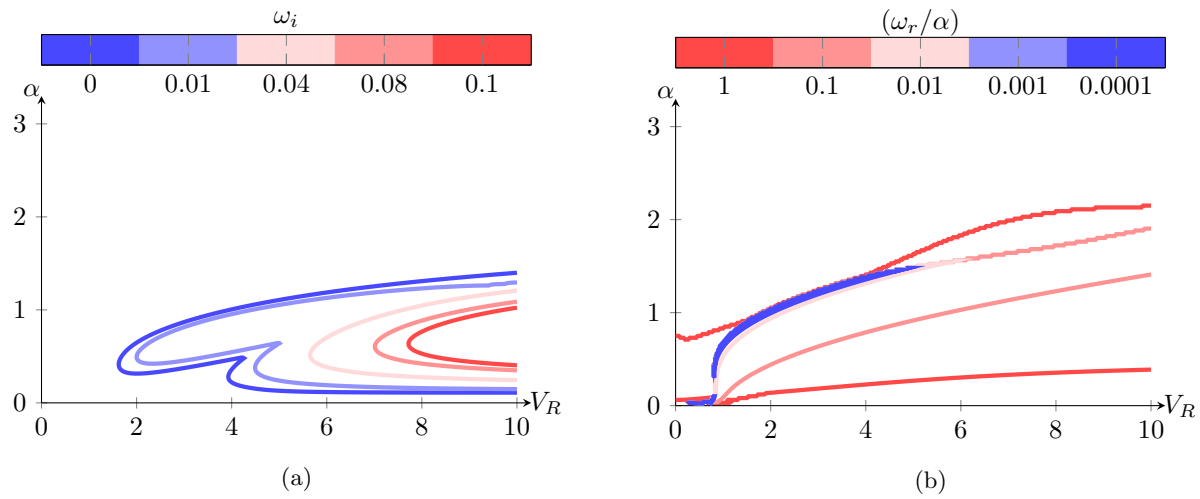

FIG. 5: Dispersion relation for leading varicose mode in (V_R, α)-plane for $Re = 5000$, $d_\star = 10$ and $B_\star = 4$: (a) contours of growth rate ω_i and (b) of phase velocity ω_r/α.

4.2. Temporal growth and instability onset

The stability features of compliant channel flow configurations depend on a large number of parameters. In the previous section we have shown that the reduced velocity V_R is the main control parameter governing fluid–structure interactions, but growth rates of the different classes of modes may also to depend significantly on Reynolds number Re, wall dissipation $d_\star$ and flexural rigidity $B_\star$. In the present section, we will map out the stability characteristics by monitoring the dispersion relation in the (V_R, α)-plane for selected values of the other relevant control parameters. By taking advantage of the base-flow symmetry, sinuous and varicose perturbations may be efficiently computed and their properties are here discussed separately. We first consider perturbations of varicose symmetry, which are generally the modes most amplified by fluid–structure interactions.

Figure 5(a) shows isolines of the temporal growth rate ω_i of the leading varicose eigenmode in the (V_R, α)-plane at $Re = 5000$, $d_\star = 10$ and $B_\star = 4$. The neutral curve ($\omega_i = 0$) exhibits two distinct minima at $V_R \approx 1.6$ and $V_R \approx 3.9$. Beyond onset, a finite range of wavenumbers α display positive temporal growth rates. The associated phase-speeds ω_r/α are given in Figure 5(b). It is found that near the first minimum $V_R \approx 1.6$, modes travel with vanishingly small phase-speeds. In contrast, near the second minimum $V_R \approx 3.9$, modes travel with phase-speeds of the order of the mean base flow velocity. This behaviour is characteristic of DIV and TWF modes, which are thus each found to dominate the perturbation dynamics in distinct regions of the (V_R, α) plane for

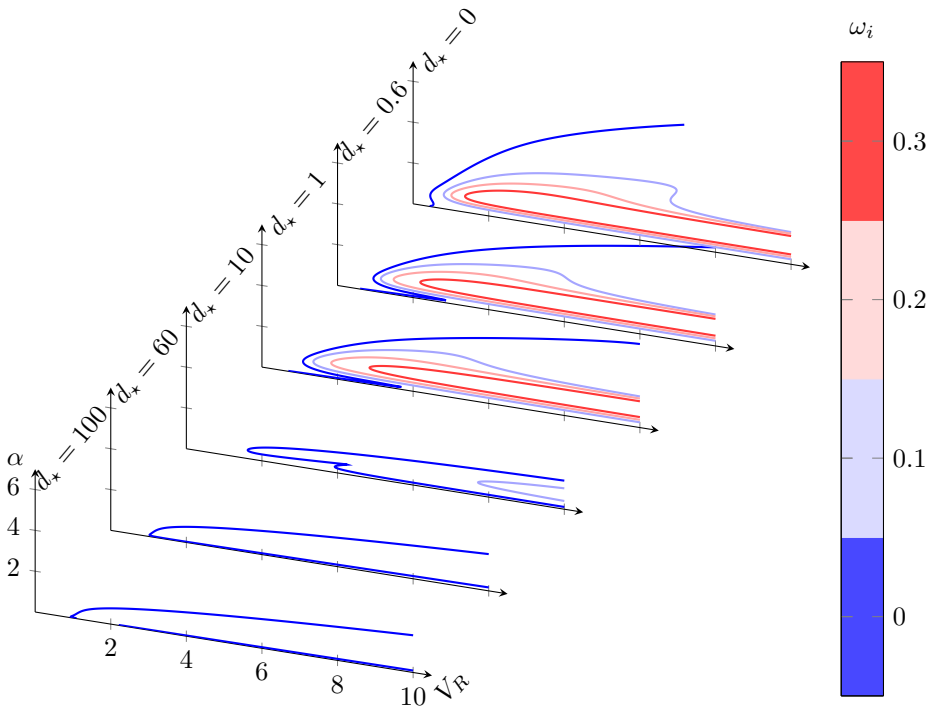

FIG. 6: Temporal growth rates ω_i for the varicose instability at $Re = 5000$ and $B_\star = 4$ for $d_\star = 0$, 0.6, 1, 10, 60 and 100. The contour levels are 0, 0.1, 0.2 and 0.3.

these parameter settings.

Figure 6 illustrates the influence of wall dissipation $d_\star$, for the same values of Re and $B_\star$. It is observed that energy dissipation in the wall only weakly influences the temporal growth rate for $0 \leq d_\star \leq 1$, while stronger stabilization occurs for $d_\star > 1$. At these high dissipation rates, the growth rate and the range of unstable wavenumbers are greatly reduced; however, the critical value of V_R for onset of instability (noted V_R^c herafter) remains of the same order of magnitude. Monitoring the neutral curves more precisely reveals that V_R^c increases from $V_R^c \simeq 0.45$ for $d_\star = 0$ to reach a maximal value of about $V_R^c \simeq 1.6$ for $d_\star = 10$ and decreases again for larger values of $d_\star$ ($V_R^c \simeq 1.0$ for $d_\star = 100$). This non-monotonous effect of wall-dissipation on instability onset is due to a change of the nature of the leading eigenmode: while the instability is dominated by the TWF mode at low values of $d_\star$, the unstable dynamics is governed by the divergence mode for strong dissipation in the compliant wall as already suggested by figure 5.

This observation is further illustrated in figure 7 where neutral curves are shown for various Reynolds numbers and wall dissipations. Especially, for $Re = 10000$ and $d_\star = 10$ (figure 7b), we observe the coexistence of the DIV and TWF modes. The critical reduced velocities V_R^c for the divergence and TWF modes are ≈ 2 and ≈ 4, respectively. Neutral curves associated with

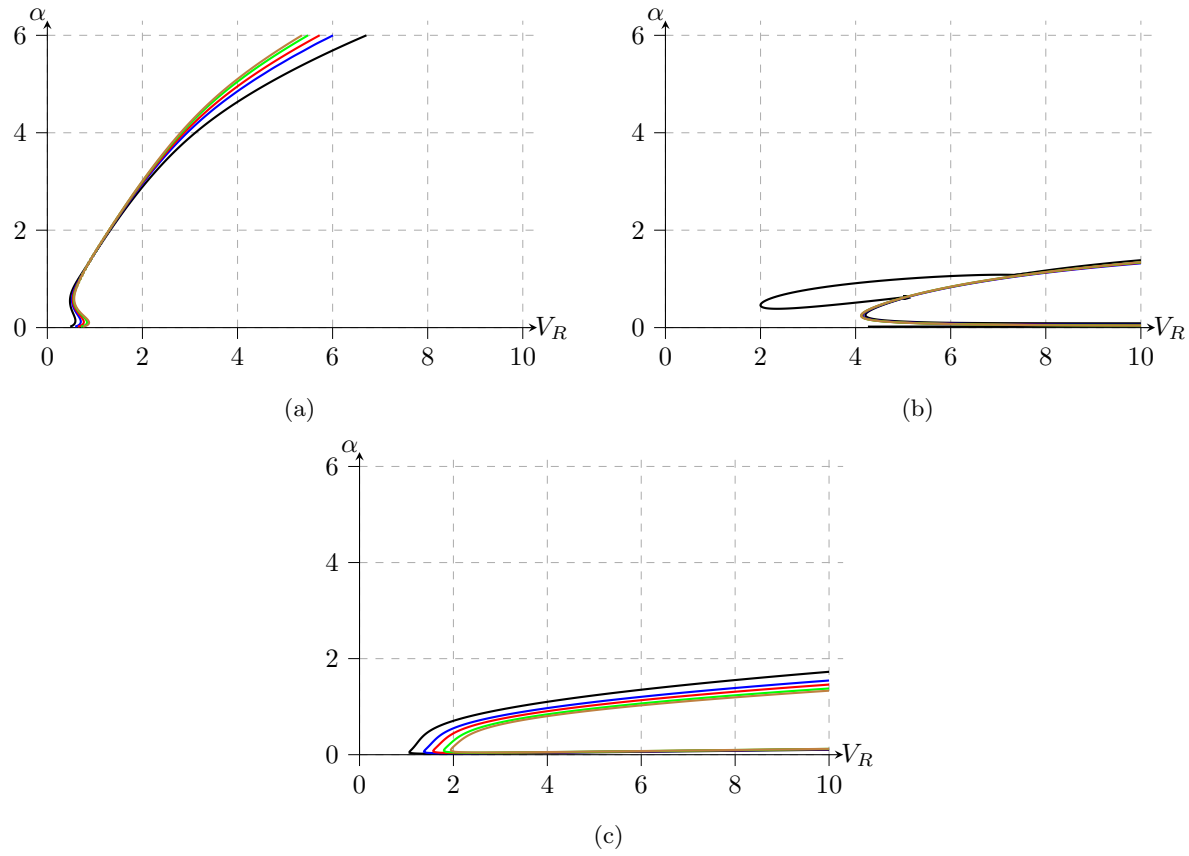

FIG. 7: Marginal curves for onset of varicose instability at $B_\star = 4$ for $Re = 10000,\ 40000,\ 80000,\ 160000$ and 240000 (in black, blue, red, green and brown respectively) and (a) $d_\star = 0$, (b) $d_\star = 10$ and (c) $d_\star = 100$.

the TWF mode (fig 7a) are seen to be almost independent of the Reynolds number. For the divergence mode, we observe a destabilizing effect of viscosity (fig 7c): the critical value V_R^c for onset of instability is seen to increase with Reynolds number, which is consistent with the fact that divergence modes are intimately connected to the viscous wall layer. Nevertheless, in the regime dominated by divergence modes, the temporal amplification rates reach much lower values than those prevailing for TWF modes at low values of $d_\star$ (see Figure 6).

The combined effects of the different wall parameters are conveniently summarized by monitoring the variations of the critical reduced velocity V_R^c. To that purpose, we consider a high value of the Reynolds number in order to focus on the influence of the wall properties. A Newton–Raphson search algorithm with an adaptive step has been implemented to identify the start of the neutral curve in the (V_R, α)-plane for different values of $d_\star$ and $B_\star$. The critical value V_R^c (and associated wavenumber α^c) for onset of instability is then obtained when $\frac{dV_R}{d\alpha}$ vanishes along the neutral curve.

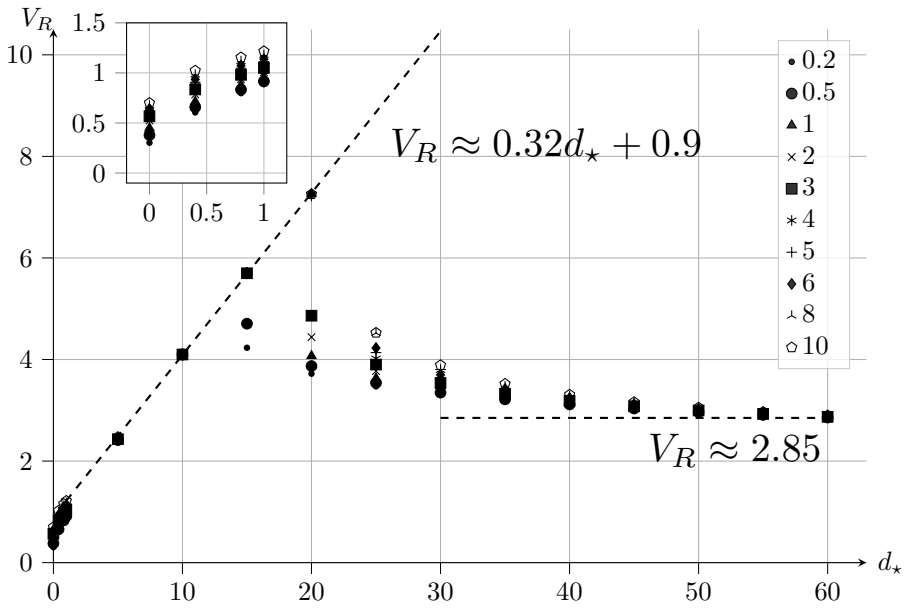

FIG. 8: Evolution of critical reduced velocity V_R^c with wall damping parameter $d_\star$, for a range of flexural ridigity values $B_\star$ (from 0.2 to 10). Perturbations of varicose symmetry are considered.

Results are reported in Figure 8 for $0 \leq d_\star \leq 60$ and $0.2 \leq B_\star \leq 10$. The inset in the figure shows that for small values of $d_\star$, flexural rigidity has a moderately stabilizing effect on TWF modes: V_R^c increases as $B_\star$ is increased for fixed $d_\star$. In the range $5 < d_\star < 15$, onset of instability is seen to display an almost universal behaviour with a linear relationship between V_R^c and $d_\star$, almost independent of $B_\star$. In this regime, instability always occurs by a TWF mode. For larger wall dissipation rates, $d_\star > 20$, the dynamics is dominated by the divergence modes, associated with vanishing phase velocities. In this latter regime, the critical values V_R^c weakly depend on flexural rigidity $B_\star$ and decrease with increasing wall dissipation $d_\star$. For large values of $d_\star$, a limit value of $V_R^c \simeq 2.85$ is asymptotically reached, independently of $B_\star$. Note that the crossover from the TWF dominated instabilities (low $d_\star$) to the DIV dominated instabilities (high $d_\star$) also depends on $B_\star$.

After the previous extensive discussions of results for varicose perturbations we now focus on the sinuous symmetry. The linear dynamics of sinuous eigenmodes is very similar to that of their varicose counterpart, except that the (sinuous) Tollmien–Schlichting modes may also display positive growth rates. The growth-rate isolines in the (V_R, α)-plane of figure 9(a) are obtained for $Re = 8000$, $B_\star = 4$ and $d_\star = 10$. This Reynolds number (based on channel diameter and mean fluid velocity) is slightly in excess of the critical value $Re_c \simeq 7696$ for Tollmien–Schlichting instability developing in rigid channel flow. As for the varicose case, the neutral curve exhibits

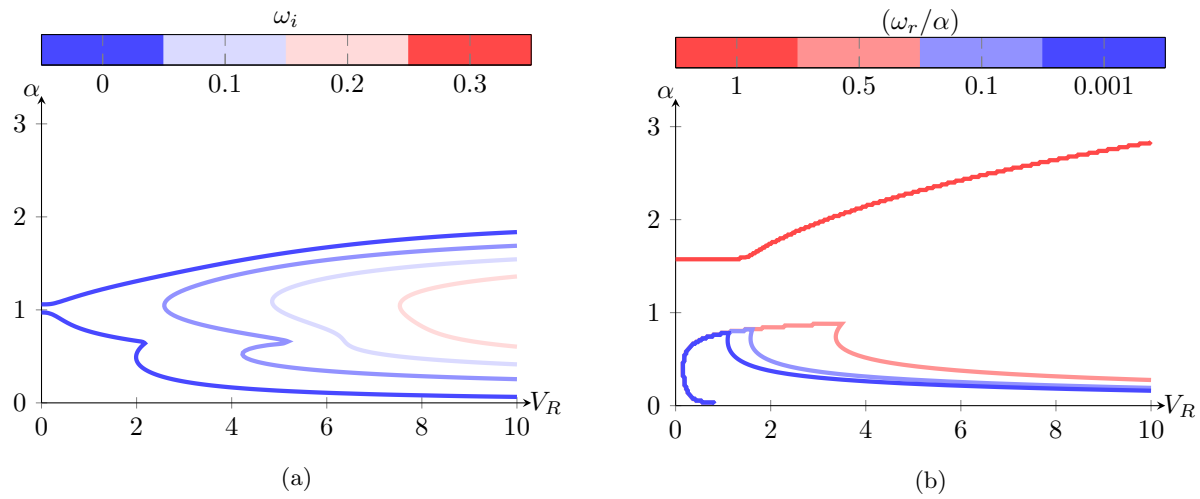

FIG. 9: Dispersion relation for leading sinuous mode in (V_R, α)-plane for $Re = 8000$, $d_\star = 10$ and $B_\star = 4$: (a) contours of growth rate ω_i and (b) of phase velocity ω_r/α.

two minima. The first appears near $V_R \approx 0$ while the second minimum is close to $V_R \approx 2$. The associated phase-speeds ω_r/α given in figure 9(b) indicate that DIV, TWF and TS modes can be involved in this regime.

Figure 10 shows the evolution of sinuous temporal instability characteristics with the wall dissipation parameter $d_\star$. For $d_\star = 0$ and low values of V_R, corresponding to near-rigid compliant walls, there exists a narrow band of unstable wavenumbers near $\alpha = 1$ associated with unstable Tollmien–Schlichting modes. At larger values of V_R, stronger fluid–structure coupling leads to the destabilization of (sinuous) TWF modes: the temporal growth rates ω_i and the range of unstable wavenumbers rapidly increase with V_R. Note that there exists a narrow region near $V_R = 1$ where both TS and TWF modes are stable. As $d_\star$ is increased from 0 to 0.6, it is observed that the regions corresponding to unstable TS and TWF modes merge, giving rise to the so-called transition mode. Therefore it appears very unlikely to successfully use wall-compliance to stabilise TS modes without destabilising TWF modes.

Except for the merging of TS and TWF instabilities, the instability features of sinuous perturbations shown in figure 10 are very similar to those observed for varicose perturbations. For $d_\star > 1$, wall dissipation $d_\star$ significantly reduces the temporal growth rates and the range of unstable wavenumbers. For $d_\star \geq 10$, figure 10 shows that divergence and transition modes co-exist. In addition, the critical reduced velocity V_R^c for the onset of the divergence mode is only weakly influenced by the wall dissipation ($V_R^c \approx 2$).

The critical curves shown in figure 11 correspond to marginal ($\omega_i = 0$) sinuous instability for

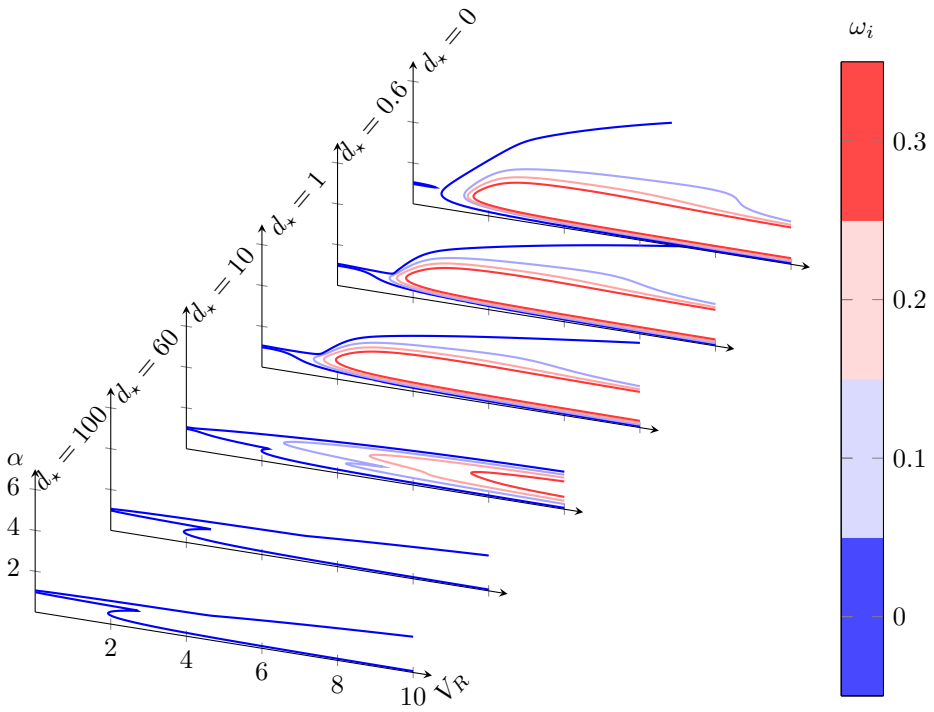

FIG. 10: Temporal growth rates ω_i for the sinuous instability at $Re = 8000$ and $B_\star = 4$ for $d_\star = 0$, 0.6, 1, 10, 60 and 100. The contour levels are 0, 0.1, 0.2 and 0.3.

a range of Reynolds numbers and $d_\star = 0$, 10 and 100. Due to the fact that, for $Re > 7696$, TS instability prevails at low values of V_R, down to $V_R = 0$, a critical value of reduced velocity V_R^c cannot be defined for onset of sinuous instability.

For the sinuous instability, it may be hard to distinguish between TS or TWF modes since branch switching occurs as some parameters are continuously varied. To better illustrate this phenomenon, figure 12 shows the dispersion relation for both branches in the range $0.55 < \alpha < 1.05$ for $d_\star = 0.10$, 0.13 and 0.16, at $Re = 1000$, $B_\star = 1$ and $V_R = 1$ For $\alpha < 0.8$, the branches with largest temporal growth rate (upper branches in figure 12a) are of TS-type while the other branches are always stable in that wavenumber range and can be identified as TWF modes. For $\alpha > 0.8$, the unstable branch displays a growth rate ω_i rapidly increasing with α, and is found to correspond to a mode of the TWF type, while the other branch is strongly stabilised at these wavenumbers. Due to the branch switching that occurs near $\alpha = 0.8$ and $d_\star = 0.13$, the unstable TWF branch prevailing for $\alpha > 0.8$ is continuously connected to the TS branch when $d_\star > 0.13$ while it is continued as a stable TWF mode for $\alpha < 0.8$ when $d_\star < 0.13$.

This behaviour is further illustrated in figure 13 where a Newton–Raphson search algorithm is used to compute neutral curves associated with either TS mode or transition mode for various

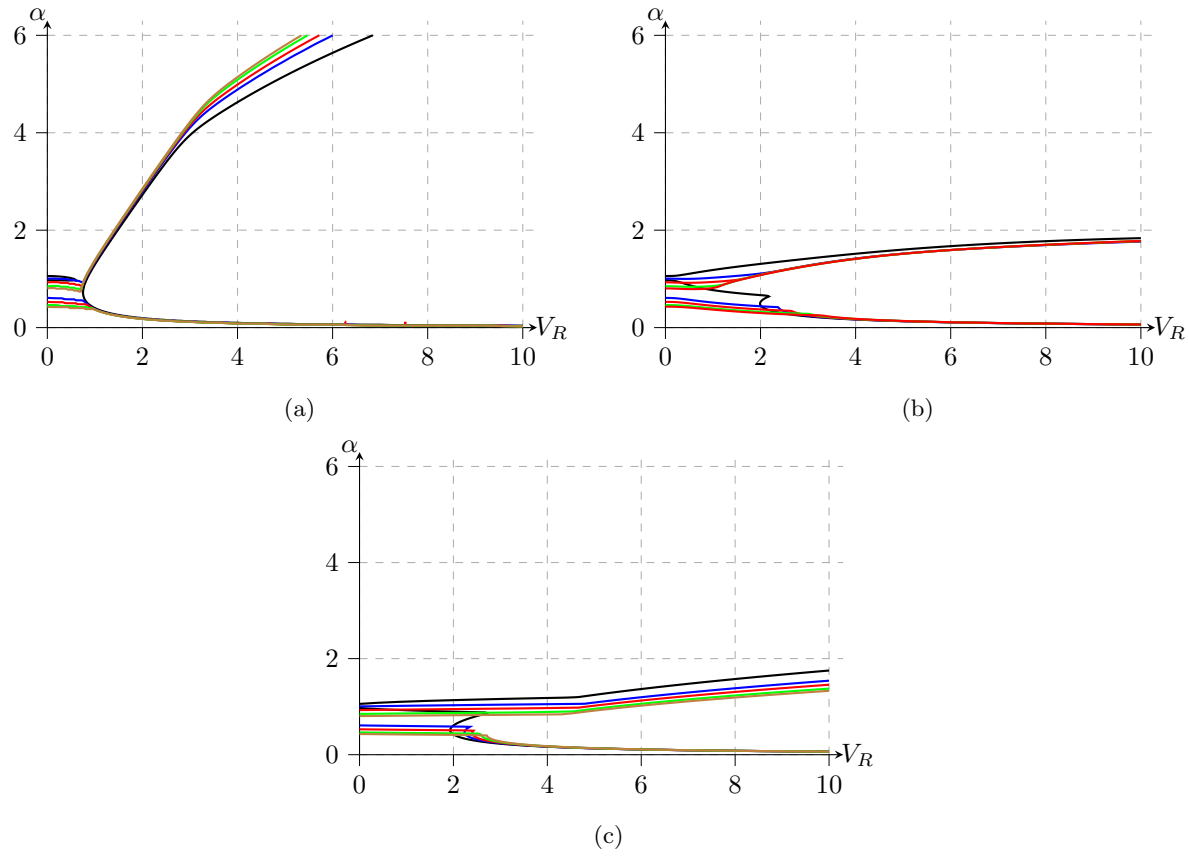

FIG. 11: Marginal curves for onset of sinous instability at $B_\star = 4$ for $Re = 10000,\ 40000,\ 80000,\ 160000$ and 240000 (in black, blue, red, green and brown respectively) and (a) $d_\star = 0$, (b) $d_\star = 10$ and (c) $d_\star = 100$.

Reynolds numbers and wall dissipations. For a small amount of wall dissipation, the TS mode is seen to be damped as V_R is increasing (figure 13a), for all the Reynolds numbers considered. In particular, for $d_\star = 0$, the critical reduced velocity of TS mode suppression is varying from $V_R \approx 0.8$ for $Re = 10000$ to $V_R \approx 4$ for $Re = 40000$. However, as $d_\star$ is increased beyond 0.13, a transition mode emerges and it is no longer possible to distinguish between TWF and TS modes (figures 13b–d).

Finally, we present some results for the destabilization of the divergence mode and its dependence on wall dissipation $d_\star$ and Reynolds number Re. We proceed as previously be computing the critical value V_R^c for onset of instability in the (V_R, α)-plane at fixed values of the other control parameters. Critical curves as functions of $d_\star$ for different Re values are plotted in Figure 14(a) and (b), respectively for the divergence modes of varicose and sinuous symmetry. Flexural rigidity is kept constant at $B_\star = 1$. Both sets of curves clearly indicate the stabilizing effect of the Reynolds

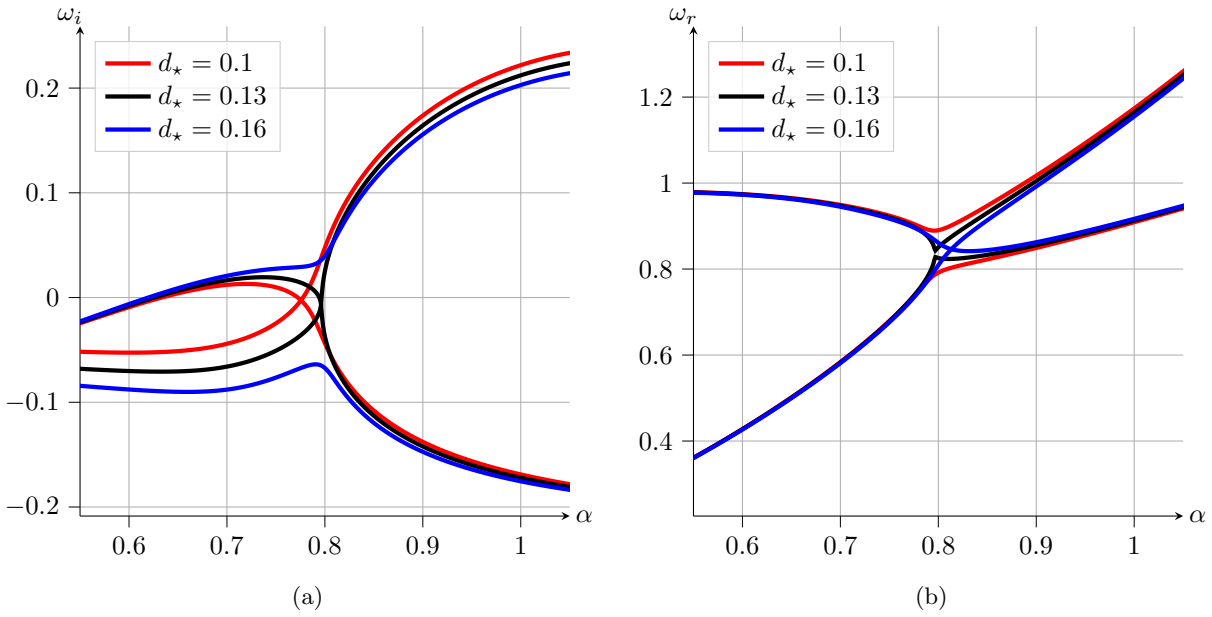

FIG. 12: Dispersion relation for the two leading sinuous modes at $Re = 10000$, $B_\star = 1$ and $V_R = 1$. (a) Temporal growth rate ω_i and (b) frequency ω_r. Branch switching occurs near $\alpha = 0.8$ and $d_\star = 0.13$.

number on the divergence mode, for both the varicose and sinuous cases. For the varicose case, unstable divergence modes only occur at relatively high wall dissipation, $d_\star > 6$ for $Re = 5000$ and $d_\star > 9.5$ for $Re = 80000$. For the sinuous case, divergence mode instability already starts for $d_\star$ in the range 2–4, with a weaker Reynolds number dependence. In both varicose and sinuous cases, the critical V_R^c appears to asymptote towards a finite limit for large values of $d_\star$.

4.3. Comparison with asymptotic theories for $d_\star = 0$

Davies & Carpenter[20] derived an analytical expression for the wall pressure for $d_\star = 0$ in the limit of small α and high Reynolds numbers, for modes of sinuous symmetry. This pressure, noted $\hat{p}(\alpha, c, U_{ref})$ is obtained as a function of the wavenumber α, the phase velocity $c = \omega/\alpha$ and a reference value for the fluid velocity $U_{ref} = Q/2h$, and includes the effects of both the critical and viscous layers. Moreover, the wall pressure is obtained as an expansion in streamwise wavenumber up to α^2: $\hat{p} = p_0 + \alpha^2 p_1$, where only the term p_1 includes the effect of viscous and critical layers. For the viscous layer, the approximation is carried out up to $O\left((\alpha Re)^{-1/2}\right)$. Neglecting the viscous stress at the wall, they obtain the dispersion relation:

$$m\left(c^2 - c_0^2\right) + \hat{p}(\alpha, c, U_{ref}) + i\left(\frac{c}{\alpha}\right) d = 0, \tag{21}$$

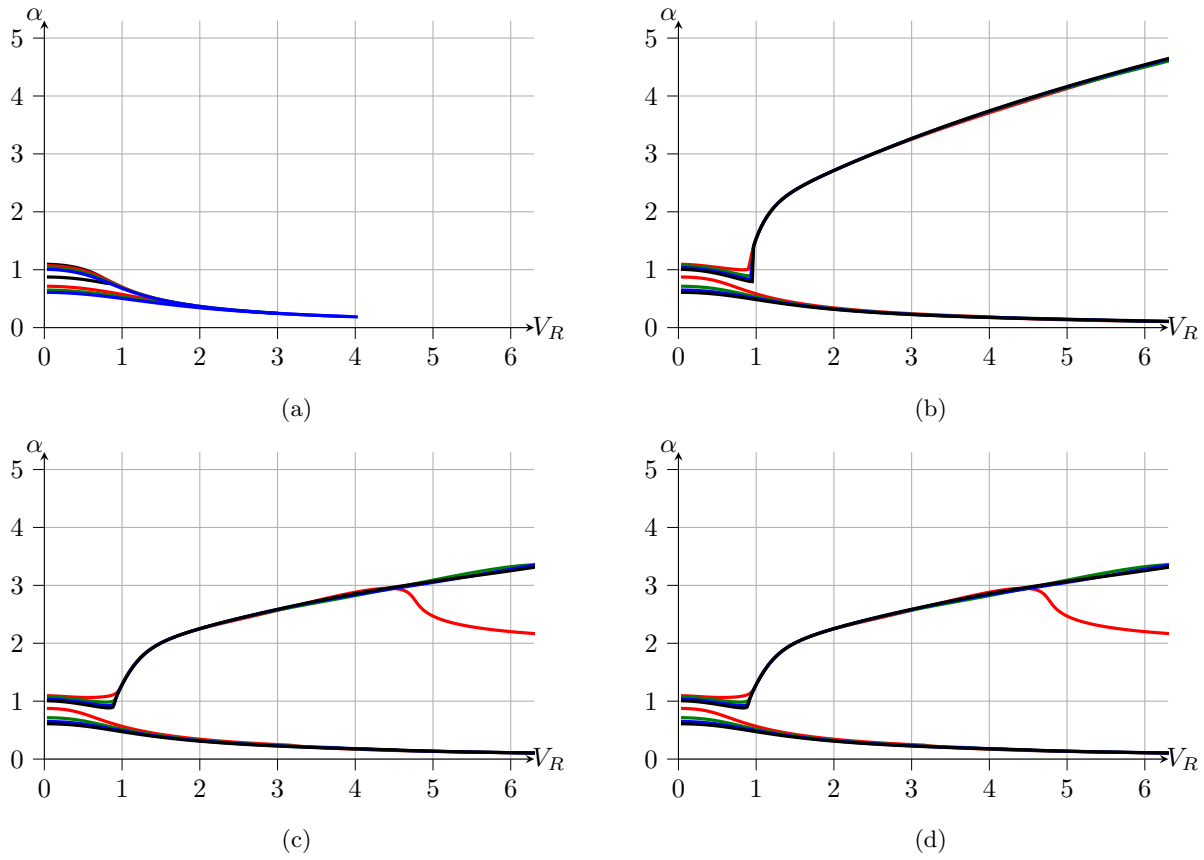

FIG. 13: Neutral curves for the TS mode for $Re = 10000,\ 20000,\ 30000,\ 40000$ (in black, red, green, blue, respectively) and $B_\star = 1$ in the plane (α, V_R). (a) $d_\star = 0$, (b) $d_\star = 0.5$, (c) $d_\star = 1$ and (d) $d_\star = 10$.

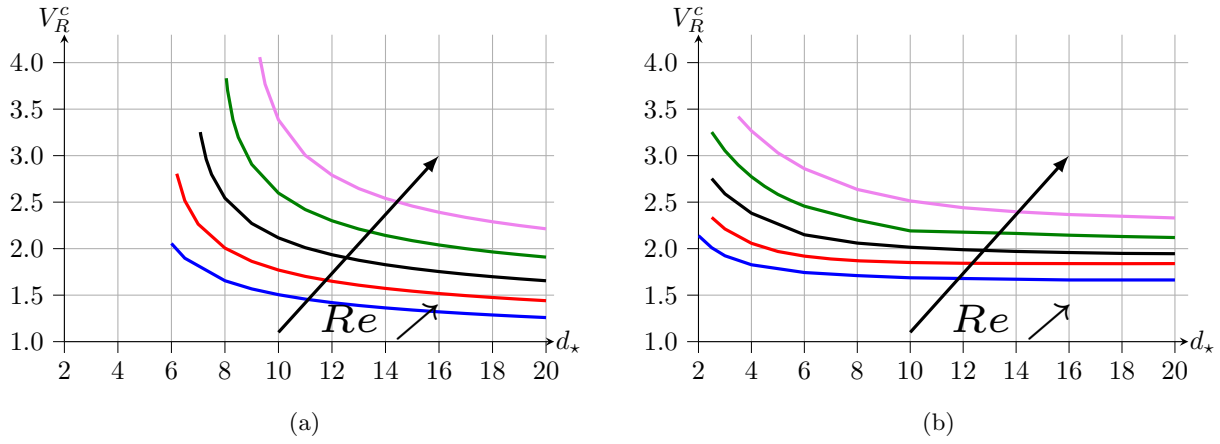

FIG. 14: Divergence mode. Critical reduced velocity distribution V_R^c with the wall damping parameter and for $Re = 5000$, 10000, 20000, 40000 and 80000 with $B_\star = 1$. (a) the varicose case, (b) the sinuous case.

with $c_0 = \sqrt{\frac{1}{m}\left(B\alpha^2 + T + \frac{K}{\alpha^2}\right)}$ the free wave speed for the wall. Davies & Carpenter[20] express the onset of instability with the Reynolds number. Here, we suggest that it is more appropriate to use the reduced velocity V_R. The resulting critical curves are shown in figure 15, without wall damping and for $B_\star = 4$. For the sinuous case, panel (a) shows a very good agreement between the analytical model and complete numerical resolution of the full system up to $\alpha \approx 3$. In order to remove the Reynolds number effect, a numerical solution for $Re = 10^6$ has been carried out. For the latter case, the grid mesh is increased up to $N = 300$ in order to correctly capture both viscous and critical layers. Figure 15(a) shows that the departure from the theoretical model is due to the expansion in terms of streamwise wave number up to α^2, hence this approximation is no longer valid for α greater than 3.5 (not shown in[16]). In addition, one observes that neglecting the viscous stress at the wall and in the analytical expression of the pressure yields an almost perfect approximation of the exact dispersion relation.

In figure 15(b), comparisons with varicose cases are shown. While the theoretical model is derived only for the sinuous symmetry, it is interesting to notice that in the limit of high Reynolds numbers, the model associated with merely the critical layer gives a quite accurate description of the varicose symmetry for α varying from 0.8 to 3. For streamwise wave numbers greater than 4, the varicose and sinuous neutral curves fall in one single curve for all Reynolds numbers. For $\alpha < 0.8$, the varicose case exhibits a more complex Reynolds number dependence. Since the varicose mode always dominates over the sinuous mode, the critical value V_R^c for onset of instability is associated with a varicose perturbation for all configurations that have been considered in the present study. The latter observation is also in agreement with results provided by Nagata[24]. In addition, it is found that the Reynolds number also has a slight stabilizing effect. In figure 15, we also provide a comparison with the theoretical model derived by Huang[34] for the varicose symmetry, only based on the critical layer. The figure also shows a good agreement for moderate values of α between the model and the numerical simulation.

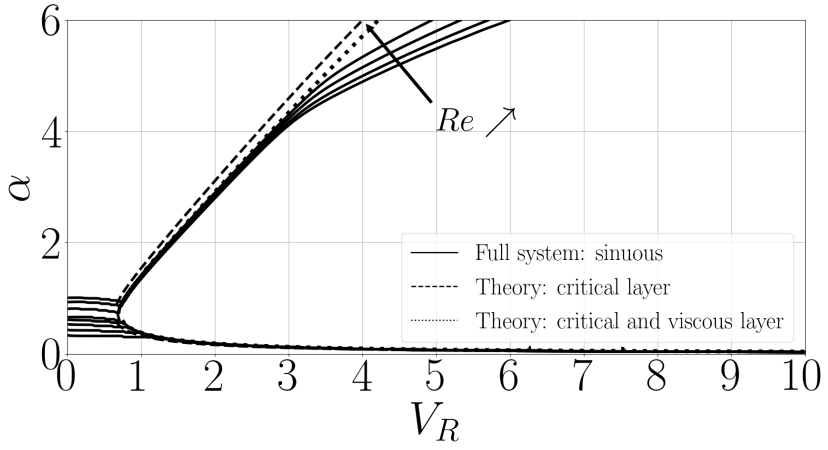

(a)

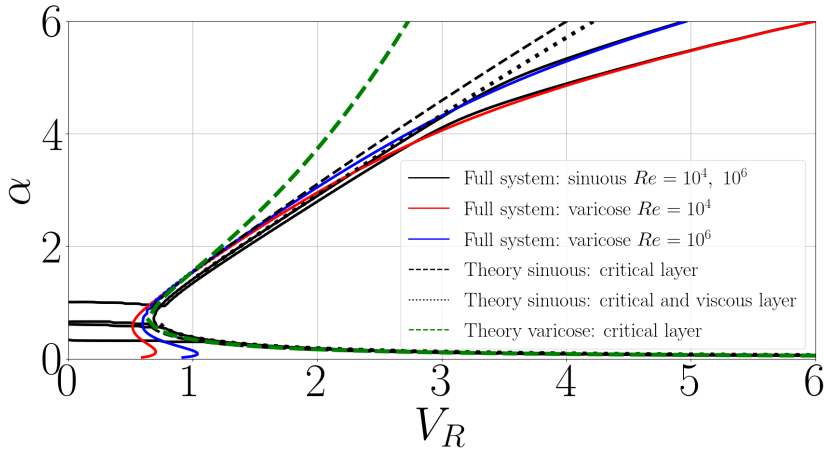

(b)

FIG. 15: Neutral curves for $d_\star = 0$ and $B_\star = 4$. For the full system of equations, the Reynolds numbers are fixed to $Re = 4 \times 10^4,\ 8 \times 10^4,\ 2.4 \times 10^5$ and 10^6. For the analytical dispersion relation including the viscous layer effect, the Reynolds number is fixed to 10^6. (a) Sinuous case, (b) Sinuous and varicose cases comparison.

4.4. Energy budgets

This final section addresses the energy transfer mechanisms between the different components of the compliant channel flow configurations, in order to shed further light on the dynamics and on the fundamental mechanisms promoting instability. We are greatly influenced by the work of Domaradski and Metcalfe[26] who carried out a similar investigation for perturbations developing in the boundary-layer flow over spring-backed membranes. A similar study was also considered by Carpenter and Morris[35] when accounting for the effect of anisotropic wall compliance on boundary layer instabilities.

For the compliant channel flow configuration under consideration, the total energy of the system is the sum of three components:

$$E_{tot} = E_{FK} + E_{WK} + E_{WP}, \tag{22}$$

where E_{FK} represents the fluid kinetic energy, while the wall energy consists of both kinetic and potential contributions, E_{WK} and E_{WP} respectively.

The global fluid kinetic energy is obtained by integration over the channel diameter

$$E_{FK} = \int_{-h}^{+h} e(y)dy, \tag{23}$$

where

$$e(y) = \rho\, \hat{\mathbf{u}}(y) \cdot \hat{\mathbf{u}}(y)^* \equiv \rho\, [\hat{u}(y)\hat{u}(y)^* + \hat{v}(y)\hat{v}(y)^*] \tag{24}$$

denotes the local kinetic energy of the flow, averaged over x at a given wall-normal position y, using the notations introduced in §2.3. The temporal variation of the local kinetic energy then follows from the governing equation (10) as

$$\begin{aligned} 2\omega_i\, e(y) = \quad & \underbrace{-\rho\, [\hat{u}(y)\hat{v}(y)^* + \hat{u}(y)^*\hat{v}(y)]\, \frac{dU_b(y)}{dy}}_{\mathcal{P}\text{: Reynolds stress work against the mean shear}} \quad \underbrace{-\frac{d}{dy}\, [\hat{p}(y)\hat{v}(y)^* + \hat{p}(y)^*\hat{v}(y)]}_{\Pi\text{: Pressure diffusion}} \\ & \underbrace{-2\mu \left[\frac{d\hat{u}(y)}{dy}\frac{d\hat{u}(y)^*}{dy} + \frac{d\hat{v}(y)}{dy}\frac{d\hat{v}(y)^*}{dy} + \alpha^2\, (\hat{u}(y)\hat{u}(y)^* + \hat{v}(y)\hat{v}(y)^*) \right]}_{\varepsilon\text{: Viscous dissipation}} \\ & \underbrace{+\mu \frac{d}{dy} \left[\hat{u}(y)\frac{d\hat{u}(y)^*}{dy} + \hat{u}(y)^*\frac{d\hat{u}(y)}{dy} + \hat{v}(y)\frac{d\hat{v}(y)^*}{dy} + \hat{v}(y)^*\frac{d\hat{v}(y)}{dy} \right]}_{\mathcal{D}\text{: Viscous diffusion}} \end{aligned} \tag{25}$$

and is the result of four distinct mechanisms as indicated in the above equation. Integration of this expression over the channel diameter leads to the equivalent equation governing the evolution of the total fluid kinetic energy,

$$\begin{aligned} 2\omega_i E_{FK} = & -\int_{-h}^{+h} \rho[\hat{u}(y)\hat{v}(y)^* + \hat{u}(y)^*\hat{v}(y)]\frac{dU_b(y)}{dy}\mathrm{d}y - \left[\hat{p}(y)\hat{v}(y)^* + \hat{p}(y)^*\hat{v}(y)\right]_{-h}^{+h} \\ & -2\mu \int_{-h}^{+h} \left[\frac{d\hat{u}(y)}{dy}\frac{d\hat{u}(y)^*}{dy} + \frac{d\hat{v}(y)}{dy}\frac{d\hat{v}(y)^*}{dy} + \alpha^2\big(\hat{u}(y)\hat{u}(y)^* + \hat{v}(y)\hat{v}(y)^*\big) \right] \mathrm{d}y \\ & +\mu \left[\hat{u}(y)\frac{d\hat{u}(y)^*}{dy} + \hat{u}(y)^*\frac{d\hat{u}(y)}{dy} + \hat{v}(y)\frac{d\hat{v}(y)^*}{dy} + \hat{v}(y)^*\frac{d\hat{v}(y)}{dy} \right]_{-h}^{+h}. \end{aligned} \tag{26}$$

While interaction with the base shear flow and viscous dissipation prevails throughout the channel cross-section, pressure and viscous diffusion only contribute at the boundaries and transfer energy between the fluid and the compliant walls.

The kinetic and potential energies associated with the walls are obtained as

$$E_{WK} = m|\omega|^2 \left(|\hat{\eta}^+|^2 + |\hat{\eta}^-|^2\right) \quad \text{and} \quad E_{WP} = \left(B\alpha^4 + T\alpha^2 + K\right)\left(|\hat{\eta}^+|^2 + |\hat{\eta}^-|^2\right), \tag{27}$$

respectively. Using the wall equations (15), together with the boundary conditions (14), yields the temporal variation of the wall energy as

$$\begin{aligned} 2\omega_i(E_{WK} + E_{WP}) = &\underbrace{-2d|\omega|^2\left(|\hat{\eta}^+|^2 + |\hat{\eta}^-|^2\right)}_{E_0} + \underbrace{\left[\hat{p}(y)\hat{v}(y)^* + \hat{p}(y)^*\hat{v}(y)\right]_{-h}^{+h}}_{E_1} \\ &\underbrace{-\mu\left[\hat{v}(y)\frac{d\hat{v}(y)^*}{dy} + \hat{v}(y)^*\frac{d\hat{v}(y)}{dy}\right]_{-h}^{+h}}_{E_2}. \end{aligned} \tag{28}$$

Thus, changes in total wall energy are seen to be the result of either dissipation within the wall (E_0) or energy exchange at the interface between the fluid and the compliant walls: work done by the pressure force (E_1) or the normal viscous stress (E_2). Both terms E_1 and E_2 also appear in (26) but with opposite sign; these fluid–structure interaction terms only account for an exchange of energy between the fluid and the walls but do not modify the total energy of the system.

The temporal variation of the total energy (22) is then obtained by adding (26) and (28), which leads to the following integrated total energy budget:

$$\begin{aligned} 2\omega_i E_{tot} = &\underbrace{-\int_{-h}^{+h}\rho\left[\hat{u}(y)\hat{v}(y)^* + \hat{u}(y)^*\hat{v}(y)\right]\frac{dU_b(y)}{dy}\mathrm{d}y}_{C_1\text{: Energy exchange with the base flow}} \\ &\underbrace{-\mu\left[\left(\frac{d\hat{u}(y)}{dy}\hat{\eta}^* + \frac{d\hat{u}(y)^*}{dy}\hat{\eta}\right)\frac{dU_b(y)}{dy}\right]_{-h}^{+h}}_{C_2\text{: Energy exchange with the base flow at the walls}} \\ &\underbrace{-2\mu\int_{-h}^{+h}\left[\frac{d\hat{u}(y)}{dy}\frac{d\hat{u}(y)^*}{dy} + \frac{d\hat{v}(y)}{dy}\frac{d\hat{v}(y)^*}{dy} + \alpha^2\left(\hat{u}(y)\hat{u}(y)^* + \hat{v}(y)\hat{v}(y)^*\right)\right]\mathrm{d}y}_{C_3\text{: Viscous dissipation}} \\ &\underbrace{-2d|\omega|^2\left(|\hat{\eta}^+|^2 + |\hat{\eta}^-|^2\right)}_{C_4\text{: Wall damping}}. \end{aligned} \tag{29}$$

Hence, the only mechanisms that contribute to variations of the total energy are interactions with the base flow and dissipation (see also[19,33]). Energy transfer from or to the base flow occurs in the bulk (C_1) as well as at the boundaries (C_2), and energy disspation takes place both in the fluid (C_3) and in the compliant walls (C_4). Note that the kinematic boundary conditions (14) have been used to bring to the fore the role of the base flow shear in the exchange term C_2. As underlined by Carpenter & Morris[35], the contribution C_2 arises from the interaction of the displaced mean flow

and shear stress. In the literature, the terms C_1 and C_2 are often labelled as irreversible energy transfer from the base flow to the perturbation; depending on the signs and phases of the different components in C_1 and C_2, they may have a destabilizing or a stabilizing influence.

The energy budget (29) may be used to recover the temporal growth rate as

$$\omega_i = \underbrace{\hat{C}_1 + \hat{C}_2 + \hat{C}_3 + \hat{C}_4}_{\Sigma}, \tag{30}$$

where the different contributions have been renormalized by the total energy, $\hat{C}_i \equiv C_i/(2E_{tot})$. Apart from physical insight into the role of the dissipation and exchange terms of the total energy, the equation (30) also provides a check of the accuracy and consistency of the numerical computations.

Now that we have identified the different components that contribute to the variation of the perturbation energy, we proceed to analyze their role in the dynamics of the different classes of modes that prevail in the present configuration. In sequence we will address TS, DIV and TWF modes and discuss the corresponding total energy budget as well as the spatial structure of the different contributions.

First we consider the stabilization mechanism of the TS mode as the reduced velocity V_R is increased. To that purpose, we investigate configurations with $Re = 10000$, $B_\star = 1$ and $d_\star = 0$. For these typical control parameter values, the TS mode is stable for V_R in excess of approximately 0.85, as shown by the black curve in figure 13(a). To study the influence of V_R on the energy transfer mechanisms, the most unstable TS mode is considered as V_R is varied, *i.e.*, the streamwise wavenumber α is chosen to maximise the temporal growth rate ω_i for each value of V_R.

Figure 16(a) plots the components of the total energy budget as V_R is increased. The associated growth rate ω_i is also reported in the same figure. The excellent agreement between the curves of ω_i, derived from the eigenvalue problem, and of Σ, right-hand-side of equation (30), gives confidence that the computation of the different energy terms is correctly implemented. The curves in figure 16(a) show that for the range of V_R considered here, the major destabilizing contribution is due to the action of the basic velocity gradient working against the Reynolds stress ($\hat{C}_1$). However, as V_R is increased, this production term $\hat{C}_1$ is observed to decrease and to be partially balanced by $\hat{C}_2$. This suggests two stabilizing mechanisms associated with the compliant wall: one reducing the bulk production term $\hat{C}_1$ and due to a modification of the perturbation velocity profiles, and another one directly connected to the wall term $\hat{C}_2$ and due to the displaced mean flow that acts as a dissipative term here. The viscous dissipation ($\hat{C}_3$) is seen to weaken as V_R is increased, but the overall stabilizing influence dominates for increasing V_R.

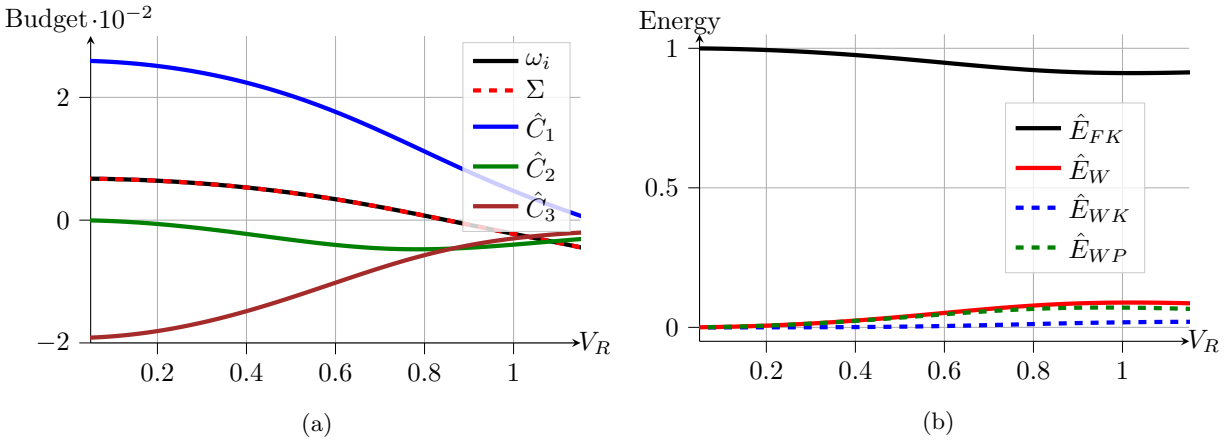

FIG. 16: Energy of most unstable TS mode as V_R is increased at $Re = 10000$, $B_\star = 1$ and $d_\star = 0$. (a) Evolution of the integrated total energy budget and comparison with temporal growth rate ω_i. (b) Different contributions to the total energy for $d_\star = 0$.

The relative importance of the different components of the total energy (22) are displayed in figure 16(b) as V_R is varied, using the notation $\hat{E}_{FK} = E_{FK}/E_{tot}$, $\hat{E}_{WK} = E_{WK}/E_{tot}$, $\hat{E}_{WP} = E_{WP}/E_{tot}$, and $\hat{E}_W = \hat{E}_{WK} + \hat{E}_{WP}$. This plot shows that, as V_R is increased, a small part of the fluid kinetic energy is indeed transferred to the wall, mainly as potential energy. This is consistent with a class A mode.

Following the work of Metcalfe & Domaradski[26], we now analyze the spatial structure of the fluid kinetic energy budget (25). Figure 17 shows the wall-normal profiles of the different contributions for the most unstable TS mode computed at different values of V_R and $d_\star$. Note that these profiles have been normalized to unit total fluid kinetic energy E_{FK}. Figures 17(a) and (b), corresponding to $V_R = 0$ and $V_R = 0.03$ at $d_\star = 0$, show that the production term $\mathcal{P}$ is significantly modified by an increase of V_R. In particular, the amplitude of $\mathcal{P}$ decreases with V_R and it exhibits a small region of negative production above the critical layer. In this region, the energy is transferred from the wave to the mean flow leading to a decrease of the total energy associated with the fluctuation. A similar observation is made by Metcalfe & Domaradski[26] for the case of a laminar boundary layer stabilized by a compliant membrane. Comparison of figures 17(a) and (b) also illustrates the importance of the viscous diffusion term $\mathcal{D}$ in redistributing energy produced by the Reynolds stress as V_R is increased, whereas the pressure diffusion term Π has a minor influence. This shows that under the action of the viscous diffusion term, the energy produced by the work of the Reynolds stress is transferred towards the wall where it is dissipated by viscosity (ε). Figure 17(a) also reveals that the production term $\mathcal{P}$ increases near the wall with the emergence of a second peak

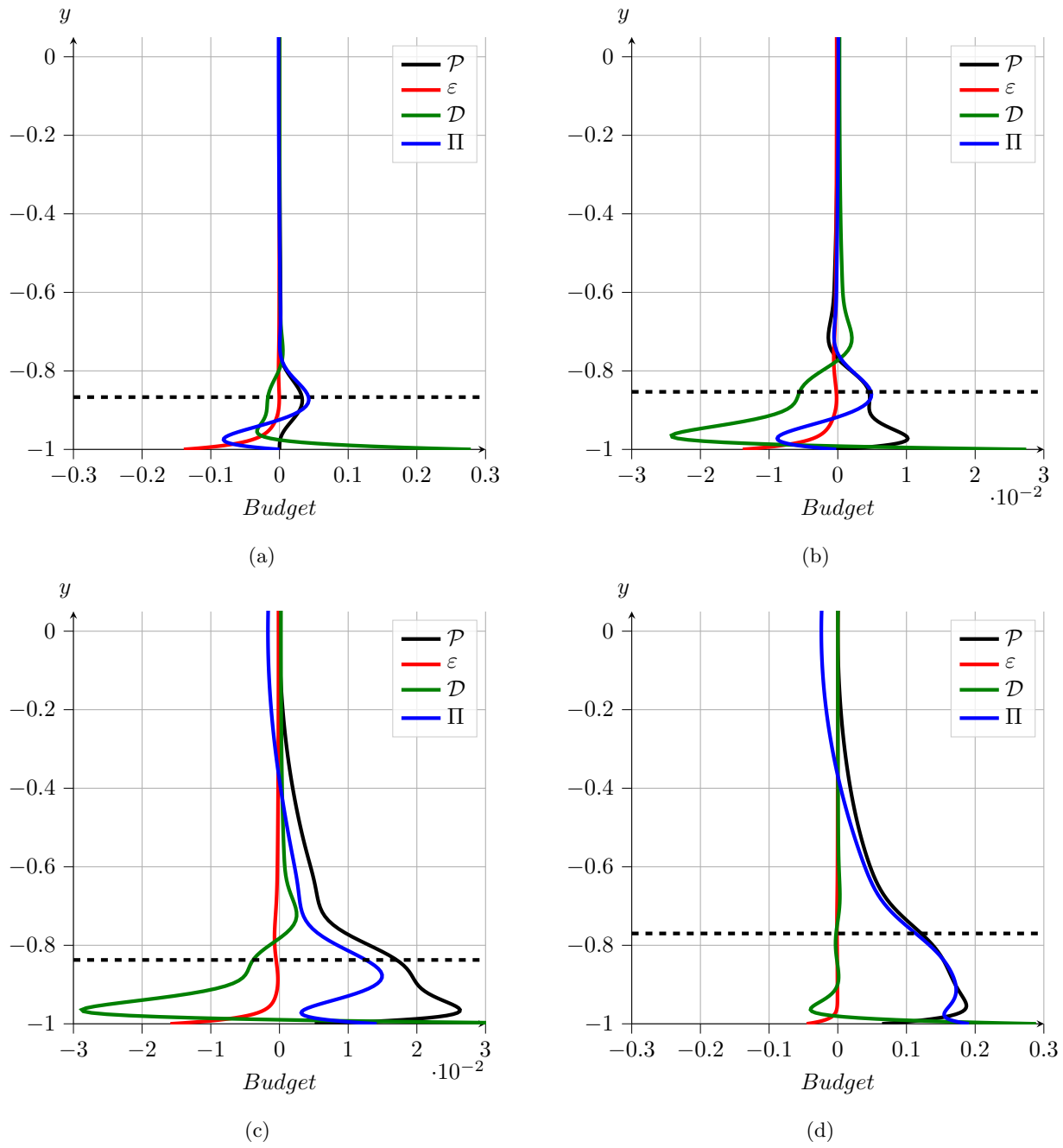

FIG. 17: Fluid kinetic energy budget profiles for most unstable TS mode at $Re = 10000$, $B_\star = 1$ and (a) $d_\star = 0$, $V_R = 0.03$, (b) $d_\star = 0$, $V_R = 1$, (c) $d_\star = 0.14$, $V_R = 1$ and (d) $d_\star = 0.2$, $V_R = 1$. The wall-normal position of the critical layer is shown in dashed line.

as V_R is increased. Due to the pressure diffusion and viscous diffusion terms, which are negatively correlated with $\mathcal{P}$, this additional production does not result in a destabilizing effect.

The influence of the dissipation within the compliant wall is illustrated in figures 17(b–d) for $V_R = 1$. When $d_\star$ is increased from 0 (b) to 0.14 (c), the TS mode is destabilized (not shown

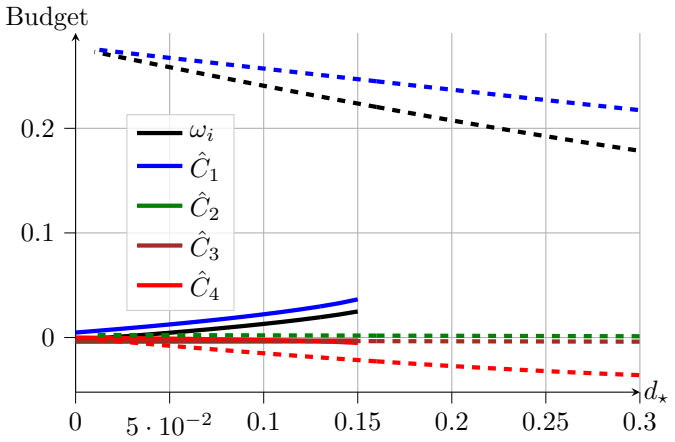

FIG. 18: Energy of most unstable sinuous modes. Evolution of the integrated total energy budget with $d_\star$ for $V_R = 1$. TS mode is shown in full line. Sinuous TWF mode is shown in dashed lines. At $d_* \approx 0.15$ modes collapse.

here for the sake of conciseness). In figure 17(c), the pressure-diffusion term Π is positive across the entire channel, which leads to work of the pressure force at the walls; the viscous diffusion profile $\mathcal{D}$ is mostly unchanged, but the peak near the wall of the production term $\mathcal{P}$ becomes the dominant feature. The increase of the dissipation leads to increase the production term in the viscous layer which is consistent with the TS mode (i.e. the phase shift mainly occurs in this region).

Finally, for a stronger wall damping $d_\star = 0.2$ (figure 17d), the pressure diffusion term Π is almost identical to the production term $\mathcal{P}$, in contrast with what is observed for $d_\star = 0.14$ and $d_\star = 0$. In particular, Π exhibits positive values near the wall which are associated with work of the pressure at the wall. This indicates that the mode is then in strong interaction with the wall and could probably be classified as a TWF mode. In particular, at $d_\star = 0.15$, a branch switching occurs and a collapse between TS and TWF mode is observed. This behaviour is illustrated in figure 18. In the figure, α is chosen to maximise ω_i for each value of $d_\star$. On one hand, for $d_\star < 0.15$ where TS mode exists, the production term $\hat{C}_1$ is increasing with the dissipation. It has for consequence to increase the temporal amplification rate of the TS mode in agreement with class A modes. On the other hand, for $d_\star > 0.15$, the temporal amplification rate is decreasing with the wall dissipation. This further indicates that beyond $d_\star = 0.15$, the mode is mainly associated with a TWF instability.

After the discussion of the TS modes, we now address the total energy budgets prevailing for DIV modes, of both sinuous and varicose symmetry. The evolution of the energy transfer mechanisms is monitored as $d_\star$ is varied, since this is the main control parameter influencing

the dynamics of DIV modes. Figure 19 shows data computed over the range $0 < d_\star < 10$ at $Re = 10000$, $B_\star = 1$ and $V_R = 2$. The evolution with $d_\star$ of the different terms of the energy budget for sinuous (figure 19a) and varicose (figure 19c) modes reveals that the term $\hat{C}_2$ dominates for both symmetries. This term accounts for the energy exchange with the base flow due to wall displacement, which is therefore identified as the main mechanism promoting instability of the DIV modes. It also confirms the influence of the Reynolds number onto the divergence mode as observed in the previous section. The importance of viscous effects for divergence modes has also been observed by Carpenter & Morris[35] for the case of a boundary-layer interacting with a compliant wall. The destabilizing effect of $\hat{C}_2$ is partially balanced by the work of the Reynolds stress against the basic shear $\hat{C}_1$, the viscous dissipation $\hat{C}_3$ and the wall dissipation $\hat{C}_4$. Hence, it illustrates the dual nature of viscous effects for the divergence mode. On one hand, it promotes the instability by propagating the energy production from the wall displacement into the flow domain, but on the other hand, viscosity also plays its usual dissipative role. Inspection of the different contributions to the total energy (figure 19b,d) shows that while the fluid energy remains the main factor in both situations, the varicose modes involve significantly more wall energy than their sinuous counterparts. Due to the slow dynamics of these modes, the wall energy is almost entirely made up of potential energy for both symmetries. It should also be mentioned that due to the long wavelengths of the DIV modes, the main contribution to the wall potential energy E_{WP} (27) is here due to the stiffness while the flexural rigidity only plays a marginal role.

The cross-channel profiles of the fluid kinetic energy budgets for the divergence modes are shown in figure 20. The figure demonstrates that the production, diffusion and dissipation contributions are all localized in the near wall region. Comparison of figures 20(a) and (b) reveals a notable difference between sinuous and varicose modes at $d_\star = 5$: while the production term $\mathcal{P}$ is negative throughout the channel cross-section for the varicose mode, the sinuous mode exhibits a small region near the wall with positive values of the production $\mathcal{P}$. Interestingly, when $d_\star$ is further increased up to $d_\star = 9$, the plots in figure 20(c) show that then the varicose production term $\mathcal{P}$ also exhibits a weakly positive region near the wall. This change of sign of the production term appears to approximately coincide with the onset of divergence instability, *i.e.*, change of sign of the growth rate ω_i plotted in figure 19(c). Hence, while the energy budget is dominated by the term $\hat{C}_2$, it seems that the instability is also significantly influenced by $\mathcal{P}$.

These detailed analyses of the energy transfer mechanisms associated with TS and DIV modes clearly indicate that the prevailing amplification processes strongly differ for both classes.

Finally we consider TWF modes and study their energy transfer properties. For this final class

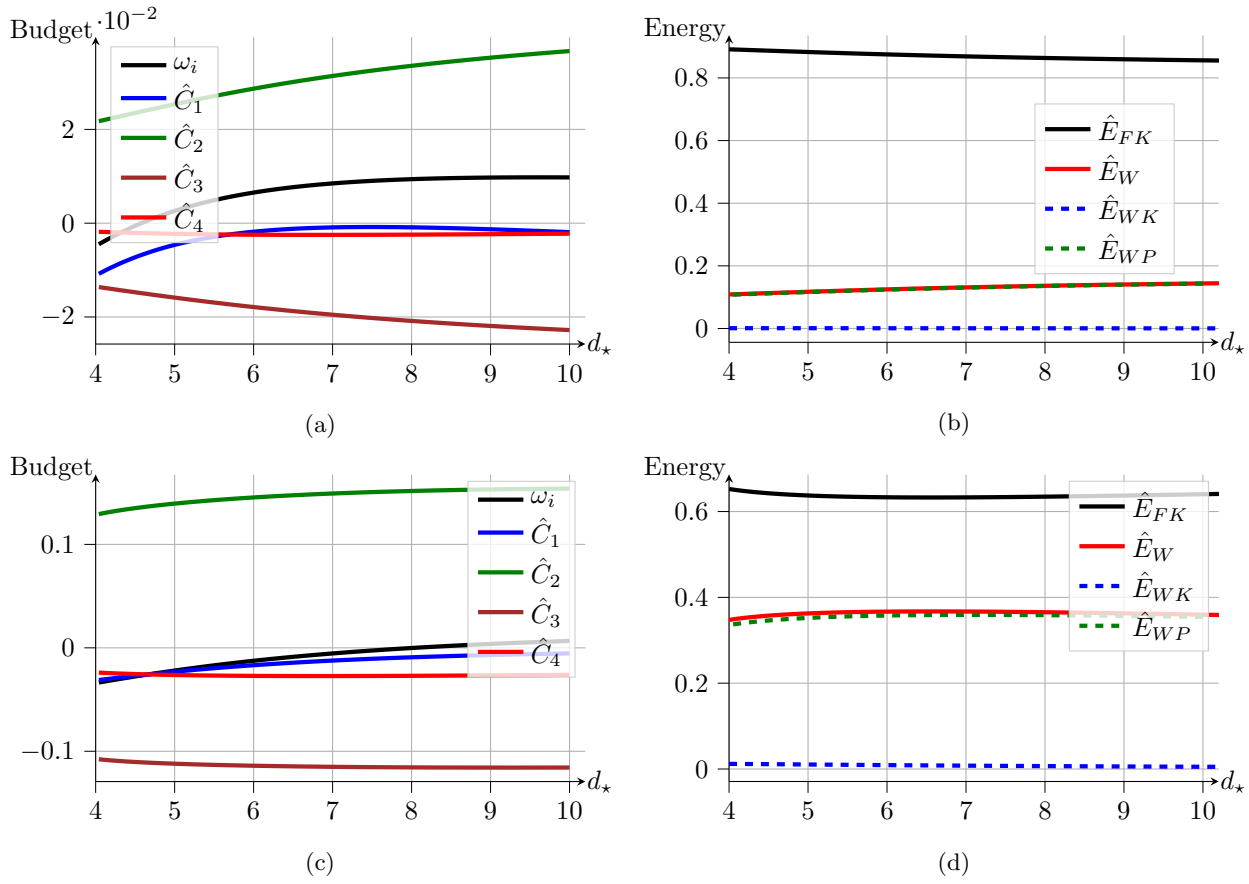

FIG. 19: Energy of most unstable DIV mode as $d_\star$ is increased at $Re = 10000$, $B_\star = 1$ and $V_R = 2$. (a,c) Evolution of integrated total energy budget and (b,d) breakdown of total energy into its components for (a,b) sinuous and (c,d) varicose modes.

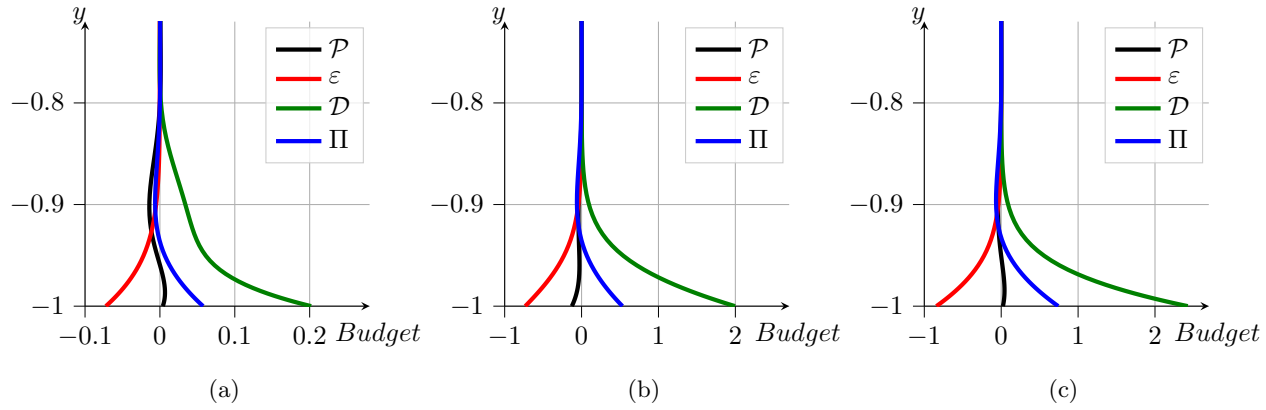

FIG. 20: Fluid kinetic energy budget profiles for most unstable DIV mode at $Re = 10000$, $B_\star = 1$ and $V_R = 2$ and (a) $d_\star = 5$ sinuous mode, (b) $d_\star = 5$ varicose mode, (c) $d_\star = 9$ varicose mode.

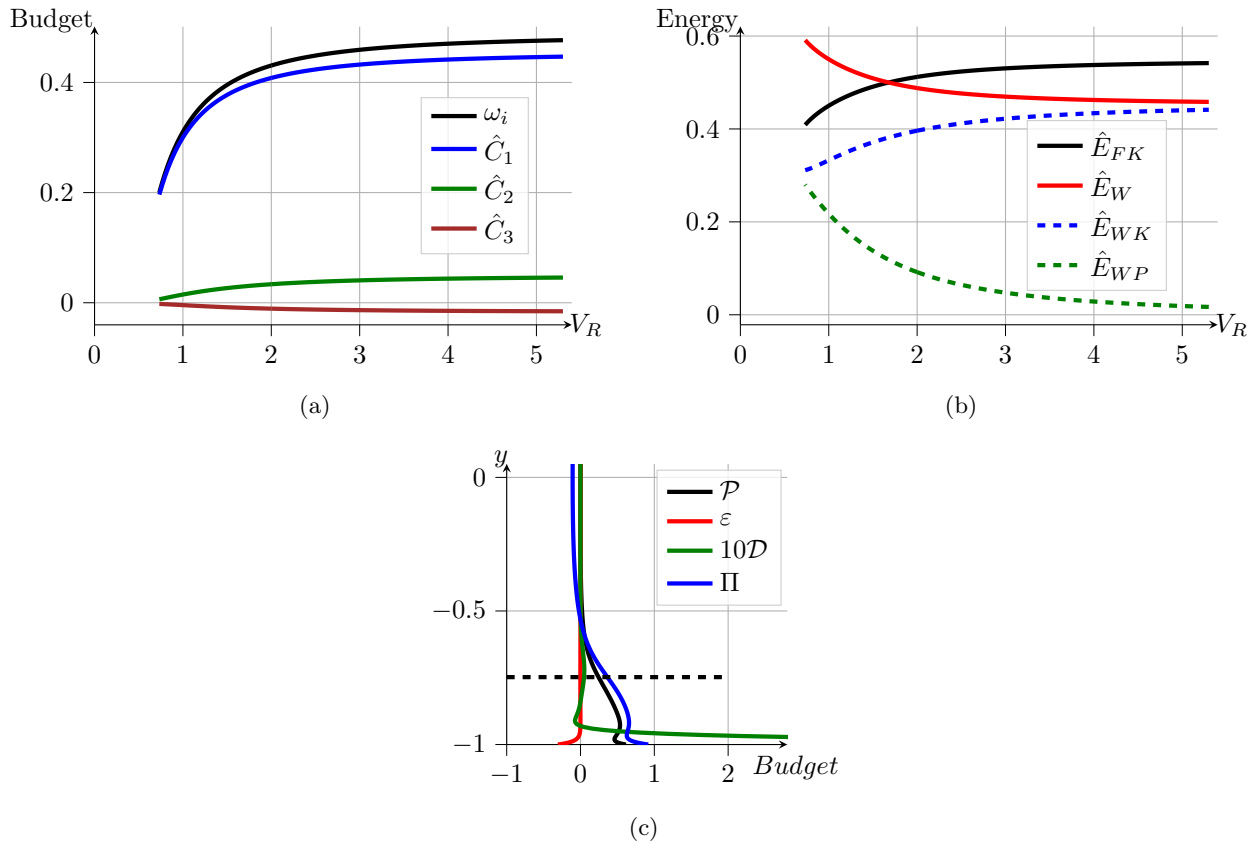

FIG. 21: Energy of most unstable varicose TWF mode as V_R is increased at $Re = 10000$, $B_\star = 1$ and $d_\star = 0$. (a) Evolution of integrated total energy budget. (b) Distribution of total energy as fluid and wall contributions. (c) Cross-channel profile of the fluid kinetic energy budget for $V_R = 3$. The wall-normal position of the critical layer is shown in dashed line.

of modes, we restrict our analysis to the varicose symmetry which has been observed to always dominate over the sinuous symmetry. The evolution of the total energy budgets with V_R is shown in figure 21(a) for $Re = 10000$, $B_\star = 1$ and $d_\star = 0$. These plots indicate that the budget is driven by the production term $\hat{C}_1$, in agreement with previous analyses[20,26]. However, it is interesting to notice that energy transfer $\hat{C}_2$ from the baseflow to the perturbation via the boundaries also promotes the instability. Both contributions $\hat{C}_1$ and $\hat{C}_2$ have a destabilizing influence. The distribution of the total energy among its different components plotted in figure 21(b) shows that for small values of V_R the wall is the most energetic component of this fluid-structure system, but for $V_R > 1.6$ the kinetic energy of the fluid overcomes the wall contribution. Thus, the present scenario appears to be exactly opposite the situation prevailing for TS modes: as V_R is increased, the ratio E_{FK}/E_W decreases for TS modes while it increases for TWF modes. This is in accordance with the

classification of TS modes as class A and TWF modes as class B modes. Finally, monitoring the potential and kinetic components of the wall energy (E_{WP} and E_{WK} respectively) shows that the wall energy is essentially due to the kinematic contribution for TWF modes, which is in contrast to the situation prevailing for DIV modes.

In figure 21(c), the fluid kinetic energy profile is shown across the channel diameter for $V_R = 3$. The role of viscosity is found to be mainly concentrated in two distinct areas. The viscous diffusion term $\mathcal{D}$ exhibits a first shallow peak around the critical layer (indicated by the dashed line), while a second stronger peak emerges near the wall due to the viscous layer. This is consistent with the theoretical model developed by Davies & Carpenter[20]. However, the dominant production term $\mathcal{P}$ is associated with the work of the Reynolds stress against the mean shear and does not exhibit a maximum near the critical layer. Its profile presents rather an inflection point near the critical layer, which is in contrast with observations by Metcalfe & Domaradski[26] for the flat plate boundary layer. We also observe that both pressure diffusion Π and viscous diffusion $\mathcal{D}$ display large positive values near the wall. Thus the energy production due to the basic shear flow is transferred to the wall through the action of both diffusion processes.

To conclude this section on energy transfer meachanisms, the influence of wall dissipation $d_\star$ is reported in figure 22 for the most unstable varicose TWF modes at $Re = 10000$, $B_\star = 1$ and $V_R = 3$. The plots in figure 22(a) show that for small values of $d_\star$ the stabilization of the TWF mode is essentially due to the increasing energy dissipation $\hat{C}_4$ in the compliant walls. For larger values of $d_\star$, both the work of the Reynolds stress against the basic shear $\hat{C}_1$ and the wall dissipation $\hat{C}_4$ evolve so as to stabilize the TWF mode. This illustrates that two distinct mechanisms are at play to diminish the growth rate for the TWF mode. The curves in figure 22(b) illustrate the redistribution of the total energy due to wall dissipation: as $d_\star$ is increased, the wall contribution (essentially kinetic energy) to the total energy decreases almost linearly in favour of the fluid contribution. The effect of the wall damping on the wall-normal profiles of the fluid kinetic energy is shown in figure 22(c). While these profiles at $d_\star = 4$ are similar to those prevailing without wall dissipation (see figure 21c), it is observed that the production $\mathcal{P}$ exhibits a lower amplitude than the pressure diffusion term Π. As $d_\star$ increases, the energy transfer from the fluid towards the wall is no longer sufficient to balance the higher wall dissipation and, as a result the proportion of fluid energy increases in the total energy of the perturbation.

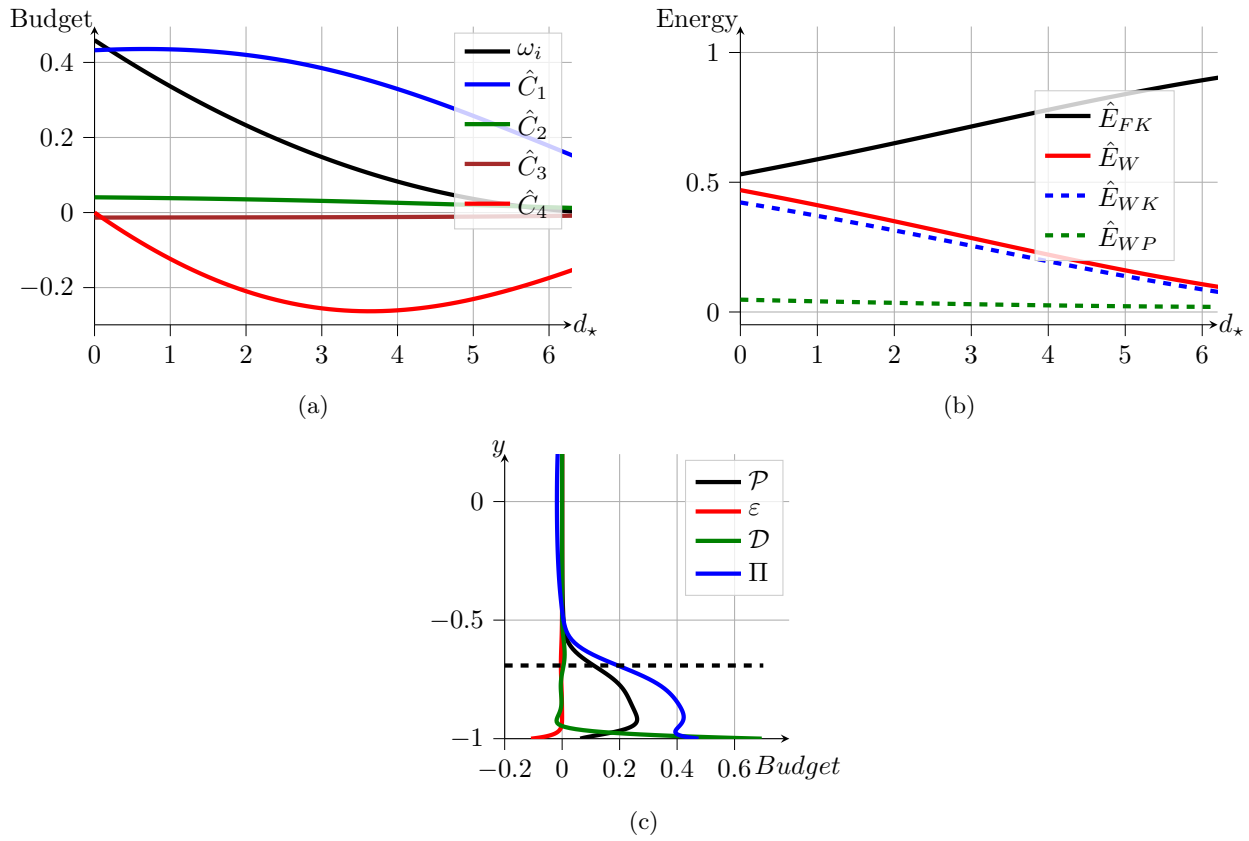

FIG. 22: Energy of most unstable varicose TWF mode as $d_\star$ is increased at $Re = 10000$, $B_\star = 1$ and $V_R = 3$. (a) Evolution of integrated total energy budget. (b) Distribution of total energy as fluid and wall contributions. (c) Cross-channel profile of the fluid kinetic energy budget for $d_\star = 4$. The wall-normal position of the critical layer is shown in dashed-line.

5. CONCLUDING REMARKS

In this study, we have revisited the linear stability problem of a fluid interacting with a compliant channel. The walls are modeled as spring-backed deformable plates including a damping mechanism. A general numerical method free of spurious pressure modes is derived to tackle this problem. By taking advantage of the base flow symmetries, varicose and sinuous eigenmodes are computed separately and efficiently. A dimensional analysis has been carried out to identify the most physically relevant control parameters. As for classical aeroelasticity problems, the main parameter is the reduced velocity (V_R), which measures the strength of the coupling between the fluid and the compliant walls. Traveling wave flutter (TWF), divergence (DIV) and Tollmien–Schlichting (TS) modes are recovered. Interestingly, the use of the reduced velocity V_R reveals that TWF modes are only weakly affected by the Reynolds number. For TWF modes, the per-

turbations of varicose symmetry are observed to be destabilized first when increasing V_R. For this symmetry, a linear relationship is found between the critical reduced velocity and the dissipation, independently of the flexural rigidity, when the wall dissipation $d_\star$ is increased. For large values of V_R, the dynamics is eventually dominated by DIV modes. For the sinuous symmetry, the TS mode is observed to depend on both V_R and Re. For $d_\star = 0$, the increase of V_R is accompanied with a damping of the TS mode as expected[7]. For the same symmetry and small values of $d_\star$, the temporal amplification rate of the TS mode is increasing, in agreement with class A mode according to Benjamin's classification[12–14]. At the same time, the TWF mode is damped. For a given value of $d_\star$, we observe the coalescence of TS and TWF modes in agreement with previous observations[7]. For both symmetries, a stabilizing effect is observed for the divergence mode when increasing the Reynolds number. This behaviour is explained through kinetic energy budget analyses.

Using a wall normal integrated energy budget, the dominant term for DIV modes appears to be associated with an irreversible energy exchange due to the interaction of the displaced mean flow and shear stress. For $d_\star = 0$, kinetic energy budgets indicate that the TS mode is stabilized as V_R is increasing under the action of two mechanisms. First, the work of the Reynolds stress against the mean flow exhibits a region above the critical layer which is negative. Here, energy is transferred from the wave to the base flow. The second mechanism is associated with an irreversible energy transfer from the fluctuation to the mean flow due to the mean flow displacement near the walls. Finally, the vertical distribution of production term associated with TWF mode is observed to peak near the walls and exhibits an inflexion point close to the critical layer for both symmetries. Hence, it shows some differences with results provided by Domaradzki & Metcalfe[26] for the boundary layer where a peak is observed near the critical layer position. Furthermore, the energy transfer from the wall to the fluid is mainly attributed to a pressure diffusion term.

Extension of the present study to non modal stability analyses can be considered in a future work. Hœpffner *et al.* [33] have investigated the same problem for three-dimensional perturbations but numerical oscillations were observed by the authors when increasing the number of eigenmodes used to compute transient growth. The formulation adopted here is free of spurious pressure modes and we believe that the problem can be solved using the numerical procedure developed in the present analysis. In addition, the role of the reduced velocity has not been investigated by Hœpffner *et al.* [33]. Finally, it should also be interesting to extend our study to pulsatile flow[36,37] and the pipe geometry which cover more biologically significant phenomena.

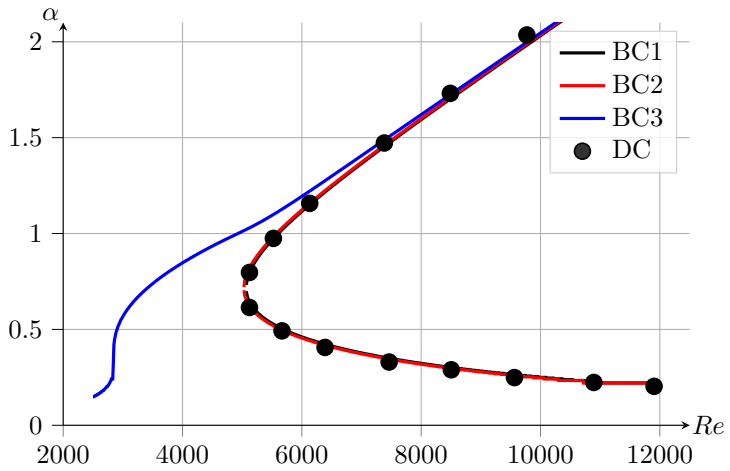

FIG. 23: Neutral curves. Sinuous configuration. Validation and illustration of the effect of the boundary conditions used for the fluid/structure interaction problem.
$K_* = 10^7,\ B_* = 4K_*,\ d_* = 0$ and $\Gamma = 2$. DC: results extracted from[20]. $BC1$: the formulation adopted in the present paper for the fluid/structure interaction problem. $BC2$: the pressure at the wall is expressed as in[20] and we neglect the viscous stress at the walls. $BC3$: formulation adopted by[25].

6. APPENDIX: VALIDATION AND INFLUENCE OF BOUNDARY CONDITIONS

For validation purposes, we adopt choices made by Davies & Carpenter[20] for dimensionless wall equations. Here, the Reynolds number is based on h, ν and the centerline velocity. The dimensionless wall parameters are

$$\Gamma = \frac{m}{\rho h},\ B_* = \frac{B}{h\rho\nu^2},\ K_* = \frac{Kh^3}{\rho\nu^2},\ d_* = \frac{dh}{\rho\nu}.$$

Davies & Carpenter[20] used an Orr–Sommerfeld equation for solving the fluid–structure interaction problem. The pressure at the lower wall is recovered through:

$$p\left(-1\right) = \frac{1}{2}\left(-i\omega\int_{-1}^{1}\hat{v}\mathrm{d}y + i\alpha\int_{-1}^{1}U_b\hat{v}\mathrm{d}y\right)$$

where the viscous terms have been neglected. For consistency, the authors have also neglected the effect of the viscous stress at the wall for the coupling between the fluid and the walls. We recall that this formulation is correct only for the sinuous configuration. Guaus *et al.* [25] used a primitive formulation for the same problem and considered only the pressure at the wall for the force associated with the fluid acting at the walls. However, the pressure is computed without

neglecting the viscous stress along the wall normal direction. In the present study, we have not neglected the effect of the viscous stress on both the pressure and the force acting onto the walls. In figure 23, we show the neutral curve for the sinuous TWF mode for $K_* = 10^7,\ B_* = 4K,\ d_* = 0$ and $\Gamma = 2$. The figure shows an almost perfect agreement between our approach and the one given by Davies & Carpenter[20]. It supports the hypotheses made by the previous authors. Nevertheless, our approach is more general because it also allows to deal with the varicose symmetry. In addition, the system also reduces to an Orr–Sommerfeld problem with only one velocity component. The figure 23 also shows that the formulation made by Guaus *et al.* [25] is not consistent and leads to discrepancies near the critical Reynolds number.

---

[1] J. B. Grotberg and O. E. Jensen. Biofluid mechanics in flexible tubes. *Annu. Rev. Fluid Mech.*, 36: 121–147, 2004.

[2] P. G. Larose and J. B. Grotberg. Flutter and long-wave instabilities in compliant channels conveying developing flows. *J. Fluid Mech.*, 331:37–58, 1997.

[3] J. Gray. Studies in anmial locomotion. VI. The propulsive powers of the dolphin. *J. Exp. Biol.*, 13: 192–199, 1936.

[4] M. Kramer. Boundary layer interactions with compliant coatings: an overview. *J. Aeronaut. Sci.*, 24: 459–505, 1957.

[5] D. M. Bushnell and K. J. Moore. Drag reduction in nature. *Annu. Rev. Fluid Mech.*, 23:65–79, 1991.

[6] F. E. Fish and G. V. Lauder. Passive and active flow control by swimming fishes and mammals. *Annu. Rev. Fluid Mech.*, 38:1923–224, 2006.

[7] M. Gad-el-Hak. Boundary layer interactions with compliant coatings: an overview. *Appl. Mech. Rev.*, 39:511–523, 1986.

[8] M. Gaster. Is the dolphin a red herring? *Turbulence Management and Relaminarisation*, Springer-Verlag, Berlin:285–304, 1988.

[9] V. Kumaran. Stability and the transition to turbulence in the flow through conduits with compliant walls. *J. Fluid Mech.*, 924:P1, 2021.

[10] R. Patne and V. Shankar. Stability of flow through deformable channels and tubes; implications of consistent formulation. *J. Fluid Mech.*, 860:837–885, 2019.

[11] J. H. Duncan. A comparison of wave propagation on the surfaces of simple membrane walls and elastic coatings bounded by a fluid flow. *J. Sound Vib.*, 119:565–573, 1987.

[12] B. Benjamin. Shearing flow over a wavy boundary. *J. Fluid Mech.*, 6:161–205, 1959.

[13] B. Benjamin. Effects of a flexible boundary on hydrodynamics stability. *J. Fluid Mech.*, 9:513–532, 1960.

[14] B. Benjamin. The threefold classification of unstable disturbances in flexible surfaces bounding inviscid flows. *J. Fluid Mech.*, 16:436–450, 1963.

[15] J. W. Miles. On the generation of surface waves by shear flows. *J. Fluid Mech.*, 3:185–199, 1957.

[16] P. W. Carpenter and A. D. Garrad. The hydrodynamic stability of flow over Kramer-type compliant surfaces. Part 1. Tollmien-Schlichting instabilities. *J. Fluid Mech.*, 155:465–510, 1985.

[17] P. W. Carpenter and A. D. Garrad. The hydrodynamic stability of flow over Kramer-type compliant surfaces. Part 2. Flow-induced surface instabilities. *J. Fluid Mech.*, 170:199–232, 1986.

[18] O. Wiplier and U. Ehrenstein. Numerical simulation of linear and nonlinear disturbance evolution in a boundary layer with compliant walls. *J. Fluids Struct.*, 14:157–182, 2000.

[19] M. Malik, M. Skote, and R. Bouffanais. Growth mechanisms of perturbations in boundary layers over a compliant wall. *Physical Review Fluids*, 3:013903, 2018.

[20] C. Davies and P. W. Carpenter. Instabilities in a plane channel flow between compliant walls. *J. Fluid Mech.*, 352:205–243, 1997.

[21] K. Tsigklifis and A. D. Lucey. Asymptotic stability and transient growth in pulsatile Poiseuille flow through a compliant channel. *J. Fluid Mech.*, 820:370–399, 2017.

[22] J. M. Rotenberry and P. G. Saffman. Effect of compliant boundaries on weakly nonlinear shear waves in channel flow. *SIAM J. Appl. Math*, 50:361–394, 1990.

[23] E. de Langre. *Fluides et Solides*. École polytechnique, 2001.

[24] M. Nagata and T. R. Cole. On the stability of plane Poiseuille flow between compliant boundaries. *Proceedings of the International Conference on Computational Methods and Experimental Measurements IX,*, WIT Press:231–240, 1999.

[25] A. Guaus and A. Bottaro. Instabilities of the flow in a curved channel with compliant walls. *Proc. R. Soc. A*, 463:2201–2222, 2007.

[26] J. A. Domaradzki and R. W. Metcalfe. Stabilization of laminar boundary layers by compliant membranes. *Physics of Fluids*, 30:695–705, 1986.

[27] V. Shankar and V. Kumaran. Stability of wall modes in fluid flow past a flexible surface. *Physics of Fluids*, 14:2324–2338, 2002.

[28] M. L. Manning, B. Bamieh, and J. Carlson. Descriptor approach for eliminating spurious eigenvalues in hydrodynamic equations. *arXiv*, 0705.1542:1–12, 2007.

[29] R. Peyret. *Spectral methods for incompressible Viscous Flow*. Springer, 2002.

[30] L. Trefethen. *Spectral Methods in matlab*. SIAM, 2000.

[31] P. J. Schmid and D. S. Henningson. *Stability and Transition in Shear Flows*. Applied Mathematical Sciences 142, Springer, 2001.

[32] P. G. Drazin and W. H. Reid. *Hydrodynamic Stability*. Cambridge University Press, 1981.

[33] J. Hœpffner, A. Bottaro, and J. Favier. Mechanisms of non-modal energy amplification in channel flow between compliant walls. *J. Fluid Mech.*, 642:489–507, 2010.

[34] L. Huang. Reversal of the Bernoulli effect and channel flutter. *J. Fluids Struct.*, 12:131–151, 1998.

[35] P. W. Carpenter and P. J. Morris. The effect of anisotropic wall compliance on boundary-layer stability and transition. *J. Fluid Mech.*, 218:171–223, 1990.

[36] B. Pier and P. J. Schmid. Linear and nonlinear dynamics of pulsatile channel flow. *J. Fluid Mech.*, 815: 435–480, 2017.

[37] B. Pier and P. J. Schmid. Optimal energy growth in pulsatile channel and pipe flows. *J. Fluid Mech.*, 2021. doi:10.1017/jfm.2021.702. in press.